Meta-analysis of Cryogenian through modern quartz microtextures reveals sediment transport histories

Jocelyn N. Reahl[1, 2], Marjorie D. Cantine[1], Julia Wilcots[1], Tyler J. Mackey[1, 3], Kristin D. Bergmann[1]

[1]Massachusetts Institute of Technology, Department of Earth, Atmospheric, and Planetary Sciences, Cambridge, Massachusetts, 02139, U.S.A.
[2]Now at the California Institute of Technology, Division of Geological and Planetary Sciences, Pasadena, California, 91125, U.S.A.
[3]Now at the University of New Mexico, Department of Earth and Planetary Sciences, Albuquerque, New Mexico, 87131, U.S.A.

Corresponding author: Jocelyn N. Reahl (jreahl@caltech.edu)

Confidential manuscript submitted to the Journal of Sedimentary Research (JSR)

1 **ABSTRACT**

2 Quantitative scanning electron microscopy (SEM) quartz microtextural analysis can

3 reveal the transport histories of modern and ancient sediments. However, because workers

4 identify and count microtextures differently, it is difficult to directly compare quantitative

5 microtextural data analyzed by different workers. As a result, the defining microtextures of

6 certain transport modes and their probabilities of occurrence are not well constrained. We used

7 principal component analysis (PCA) to directly compare modern and ancient aeolian, fluvial, and

8 glacial samples from the literature with 9 new samples from active aeolian and glacial

9 environments. Our results demonstrate that PCA can group microtextural samples by transport

10 mode and differentiate between aeolian and fluvial/glacial transport modes across studies. The

11 PCA ordination indicates that aeolian samples are distinct from fluvial and glacial samples,

12 which are in turn difficult to disambiguate from each other. Ancient and modern sediments are

13 also shown to have quantitatively similar microtextural relationships. Therefore, PCA may be a

14 useful tool to constrain the ambiguous transport histories of some ancient sediment grains. As a

15 case study, we analyzed two samples with ambiguous transport histories from the Cryogenian

16 Bråvika Member (Svalbard). Integrating PCA with field observations, we find evidence that the

17 Bråvika Member facies investigated here includes aeolian deposition and may be analogous to

18 syn-glacial Marinoan aeolian units including the Bakoye Formation in Mali and the Whyalla

19 Sandstone in South Australia.

20

21 **INTRODUCTION**

22 Scanning electron microscopy (SEM) quartz microtextural analysis reveals microscale

23 features (microtextures) that are formed during transport (Krinsley and Takahashi 1962; Krinsley

2

24   and Doornkamp 1973; Bull 1981). Because different transport modes imprint specific suites of

25   microtextures onto quartz grains, quartz microtextural analysis is a useful technique to

26   understand the transport histories of modern and ancient sedimentary deposits (Krinsley and

27   Doornkamp 1973; Mahaney 2002; Vos et al. 2014). Quantitative quartz microtextural analysis,

28   which treats microtextural data as a multidimensional statistical problem, is a particularly

29   promising method to quantify the probabilities of occurrence of each microtexture in a specific

30   transport mode (Mahaney et al. 2001; Říha et al. 2019). However, because workers identify and

31   count microtextures differently—even for sand grains from the same depositional environment

32   (Culver et al. 1983)—it is difficult to directly compare quantitative microtextural data analyzed

33   by more than one worker in the same reference frame.

34   Here we use principal component analysis (PCA) to directly compare quantitative

35   microtextural data from modern and ancient aeolian, fluvial, and glacial sediments across

36   workers. Because experimental studies have shown that certain microtextures form in specific

37   transport settings (Krinsley and Takahashi 1962; Lindé and Mycielska-Dowgiałło 1980; Costa et

38   al. 2012; Costa et al. 2013; Costa et al. 2017), we expect the PCA ordinations to distinguish

39   aeolian, fluvial, and glacial sediments from each other regardless of worker. We also hypothesize

40   that the modern and ancient samples will be quantitatively similar to each other in PCA space,

41   and that the depositional histories of ambiguous ancient sedimentary environments can be

42   constrained using this method.

43   One such case of an ambiguous ancient sedimentary environment is the Cryogenian

44   (720–635 Ma) Bråvika Member (northeastern Svalbard, Norway). The Bråvika Member is a

45   northward-thickening and coarsening-upward wedge of quartz arenite with lenses and beds of

46   dolomite (Halverson et al. 2004). Since the Bråvika Member was first recognized as a unit by

3

47 Halverson et al. (2004), there have been three prevailing hypotheses for what depositional

48 environment the Bråvika could represent:

49   1) a glaciofluvial outwash plain associated with the overlying Wilsonbreen Formation

50 (Halverson et al. 2004), which is correlated with the Marinoan "Snowball Earth" pan-glaciation

51 (Hoffman et al. 2012);

52   2) an aeolian depositional environment associated with either the glacial conditions of the

53 Wilsonbreen Formation or the tropical equatorial conditions of the underlying upper Elbobreen

54 Formation (Halverson 2011), the latter of which is correlated with the Cryogenian interglacial

55 period (Fairchild et al. 2016); or

56   3) a tropical fluvial environment associated with the upper Elbobreen Formation

57 (Hoffman et al. 2012).

58   To test if our PCA analysis method can constrain the transport histories of ambiguous

59 ancient sedimentary environments, we transformed two microtextural samples of the Bråvika

60 Member from Buldrevågen (north-northeast Spitsbergen) into the PCA ordinations. Integrating

61 the microtextural data with field observations from Buldrevågen, Geerabukta (Ny Friesland), and

62 Gimleodden (Nordaustlandet), we show that PCA is not only able to distinguish aeolian, fluvial,

63 and glacial transport modes from each other using microtextural data, but it is also able to help

64 elucidate the ambiguous transport histories of ancient sediment grains.

65

66   **MATERIALS**

67   *Modern Samples*

68   **New Modern Samples. ——** We present five new aeolian samples from the McMurdo

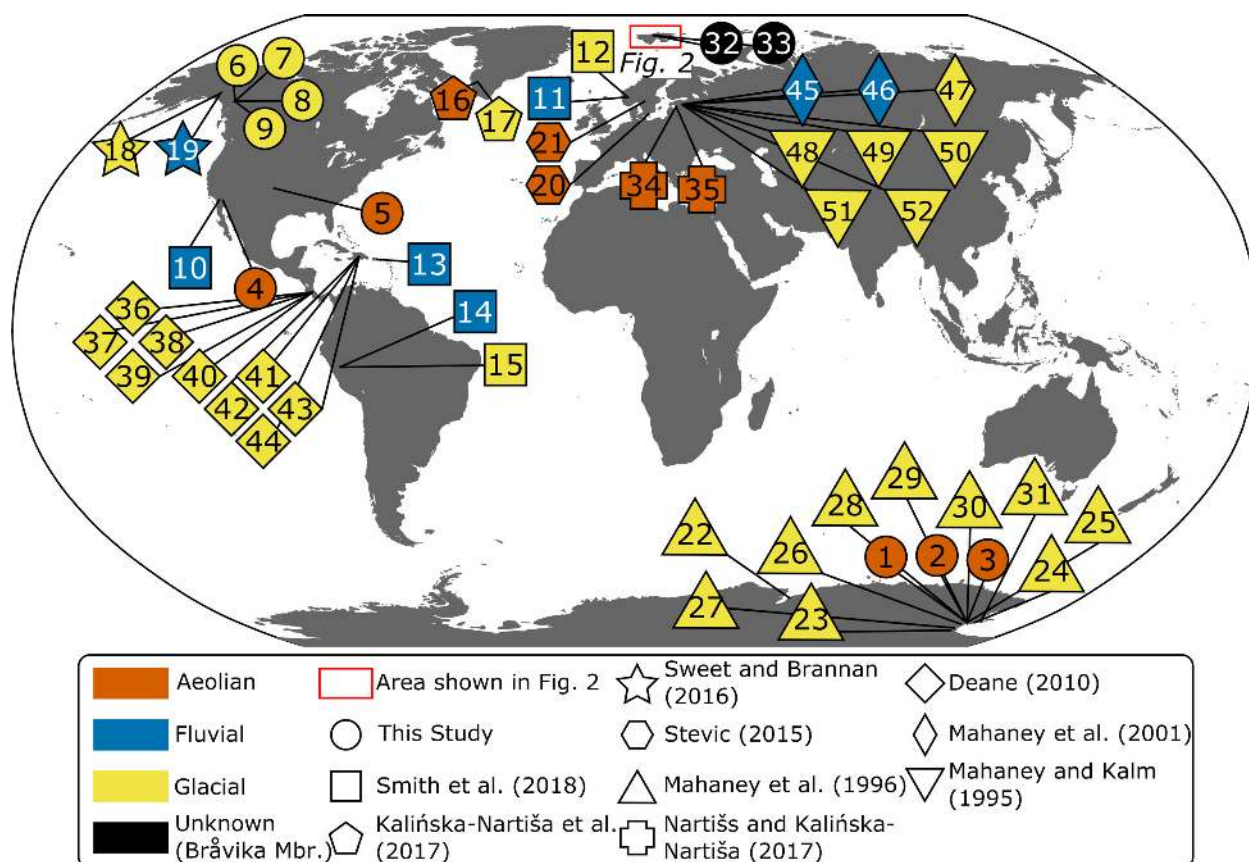69 Dry Valleys (Antarctica), Algodones Dunes of California (Cocopah (*Kwapa*), Kumeyaay, Salt

Figure 1. Global map of all samples analyzed in this study. The number in each marker corresponds to the sample group number in Tables 1 and 2.

70   River Pima-Maricopa (*O'odham-Piipaash*), and Quechan (*Kwatsáan*) territory), and Waynoka

71   Dunes of Oklahoma (Comanche (*Nʉmʉnʉʉ*), Keechi (*Ki:che:ss*), Kiowa (*[Gáui[dòñ:gyà*), Osage

72   (*Wahzhazhe*), Tawakoni (*Tawá:kharih*), Waco (*Wí:koʔ*), and Wichita (*Kirikirʔi:s*) territory), as

73   well as four new glacial samples from the Llewellyn Glacier in British Columbia on Taku River

74   Tlingit (*Lingít*) territory (Fig. 1; Table 1). Each of these samples are briefly described in the

75   following paragraphs, and more detailed descriptions can be found in the Supplementary

76   Material.

77   Of the five aeolian samples, three are sourced from perennially ice-covered lakes in the

78   McMurdo Dry Valleys: one from Lake Fryxell (documented in Jungblut et al. 2016), one from

5

Confidential manuscript submitted to the Journal of Sedimentary Research (JSR)

Table 1. List of the samples from modern depositional environments considered in this study. Each group of samples is assigned a number for later reference in Figures 1 and 5 (Column #). Column S indicates the number of samples in each sample group, and column N indicates the number of quartz grains in each sample group.

Study	#	Sample Location	Transport	S	N	GPS Point
This Study	1	Lake Fryxell, McMurdo Dry Valleys, Antarctica	Aeolian	1	31	77°36'48"S, 163°06'40"E
	2	Lake Joyce, McMurdo Dry Valleys, Antarctica	Aeolian	1	34	77°43'11"S, 161°36'25"E
	3	Lake Vanda, McMurdo Dry Valleys, Antarctica	Aeolian	1	30	77°31'38"S, 161°36'24"E
	4	Algodones Dunes, California, U.S.	Aeolian	1	44	33°08'57"N, 115°18'48"W
	5	Waynoka Dunes, Oklahoma, U.S.	Aeolian	1	48	36°33'35"N, 98°53'56"W
	6	Llewellyn Glacier, B.C. (JIF19-C26-01)	Glacial	1	31	59°00'49"N, 134°07'15"W
	7	Llewellyn Glacier, B.C. (JIF19-C26-02)	Glacial	1	39	59°00'48"N, 134°07'13"W
	8	Llewellyn Glacier, B.C. (JIF19-C26-03)	Glacial	1	36	59°00'48"N, 134°07'13"W
	9	Llewellyn Glacier, B.C. (JIF19-C26-04)	Glacial	1	40	59°00'50"N, 134°07'14"W
Smith et al. (2018)	10	Anza-Borrego Desert, California, U.S.	Fluvial	5	250	32°54'00"N, 116°16'00"W
	11	Auster and Storelvi Rivers, Norway	Fluvial	7	346	61°32'00"N, 06°57'00"E
	12	Austerdal Glacier Moraine, Norway	Glacial	1	50	61°32'00"N, 06°57'00"E
	13	Rio Guayanés, Puerto Rico	Fluvial	6	297	18°03'00"N, 65°54'00"W
	14	Rio Parón, Peru	Fluvial	5	250	09°00'00"S, 77°42'00"W
	15	Moraine Proximal to Lake Parón, Peru	Glacial	1	48	09°00'00"S, 77°42'00"W
Kalińska-Nartiša et al. (2017)	16	Russell Glacier, Greenland (CE1, CE2, CE8)	Aeolian	3	60	67°05'00"N, 50°20'00"W
	17	Russell Glacier, Greenland (CE12, CE13)	Glacial	2	40	67°07'00"N, 50°05'00"W
Sweet and Brannan (2016)	18	Chitina Glacier Moraine to 12 km Past Tana River Confluence, Alaska, U.S. (CR-1 to CR-23)	Glacial	22	626	61°05'44"N, 142°11'03"W
	19	12 km Past Tana River Confluence to the Copper River, Alaska, U.S. (CR-24 to CR-41)	Fluvial	18	450	61°21'42"N, 143°46'34"W
Stevic (2015)	20	Coastal Sand Dune, Vittskövle, Sweden	Aeolian	1	15	55°51'56"N, 14°10'02"E
	21	Inland Sand Dune, Brattforsheden, Sweden	Aeolian	1	15	59°36'26"N, 13°53'03"E
Mahaney et al. (1996)	22	Lichen Valley, Vestfold Hills, Antarctica (Site A)	Glacial	1	25	68°28'53"S, 78°10'24"E
	23	Ackerman Ridge, Scott Glacier area, Antarctica (Sites B – C)	Glacial	1	25	85°45'00"S, 153°00'00"W
	24	Southern Inexpressible Island, Antarctica (Site D)	Glacial	1	25	74°54'00"S, 163°39'00"E
	25	Taylor Glacier, McMurdo Dry Valleys, Antarctica (Site E)	Glacial	1	25	77°44'00"S, 162°10'00"E
	26	Hatherton Glacier, Antarctica (Site F)	Glacial	1	25	79°55'00"S, 157°35'00"E
	27	Roberts Massif, Antarctica (Sites G – H)	Glacial	2	50	85°32'00"S, 177°05'00"W
	28	Barwick Valley, Antarctica (Site I)	Glacial	1	25	77°23'24"S, 161°02'18"E
	29	Cambridge Glacier, Antarctica (Site J)	Glacial	1	25	76°57'00"S, 160°31'00"E
	30	Southern Inexpressible Island, Antarctica (Site D)	Glacial	1	25	75°38'00"S, 161°05'00"E
	31	Luther Peak Basin, Edisto Inlet, Antarctica (Site L)	Glacial	1	25	72°22'00"S, 169°50'00"E

6

79   Lake Joyce (documented in Mackey et al. 2015) and one from Lake Vanda (documented in

80   Mackey et al. 2017). The bulk of coarse-grained sedimentation under the ice cover of these lakes

81   is wind-blown quartz- and feldspar-rich sand that melts through the ice and is deposited within

82   layers of microbial mats on the lake floor (Gumbley 1975; Green et al. 2004; Shacat et al. 2004;

83   Jungblut et al. 2016). The lakes' lack of wind-driven turbulence (Spigel and Priscu 1998) and

84   neutral to high pH (Green et al. 2004; Shacat et al. 2004; Jungblut et al. 2016) suggest that these

85   aeolian grains are negligibly overprinted by lacustrine transport or acidification processes after

86   they melt through the ice.

87   The remaining two aeolian samples are from the Algodones Dunes and the Waynoka

88   Dunes (both documented by Adams 2018; Adams and Soreghan 2020). Both dunefields are

89   sourced from fluvial deposits (Winspear and Pye 1995; Lepper and Scott 2005) and have been

90   active since the late Holocene (Stokes et al. 1997; Lepper and Scott 2005). Given that aeolian

91   transport over short distances and timeframes rapidly imprints aeolian microtextures on quartz

92   grains (Costa et al. 2013), we expect there to be negligible fluvial overprinting on these samples.

93   The four glacial samples from the Llewellyn Glacier on the Juneau Icefield were

94   collected from lateral glacial moraines (JIF19-C26-02 and JIF19-C26-03) and an ephemeral

95   glaciofluvial melt stream 10 m downstream from a separated branch of ice from the Llewellyn

96   Glacier (JIF19-C26-01 and JIF19-C26-04; Fig. S1). Because many kilometers of fluvial transport

97   are needed to create a fluvial microtextural overprint on glacial sediment (Pippin 2016; Sweet

98   and Brannan 2016; Křížek et al. 2017), samples JIF19-C26-01 and JIF19-C26-04 are more

99   representative of a glacial setting than a fluvial setting.

100   **Modern Literature Samples.** ⸺ Previously published aeolian, fluvial, and glacial

101   samples comprise the remainder of modern samples considered in this study (Fig. 1; Table 1).

102 We selected 5 studies to use in this modern dataset: Mahaney et al. (1996), Stevic (2015), Sweet

103 and Brannan (2016), Kalińska-Nartiša et al. (2017), and Smith et al. (2018).

104 Mahaney et al. (1996) analyzed 11 glacial samples distributed around the Antarctic

105 continent. Stevic (2015) analyzed two aeolian samples, one from a coastal dune in Vittskövle,

106 Sweden and another from an inland sand dune near Brattforsheden, Sweden. Sweet and Brannan

107 (2016) investigated the microtextural transition from glacially-dominated samples to fluvially-

108 dominated ones using 46 samples of sand collected along a transect from the Chitina Glacier to

109 the Copper River in Alaska. For the purposes of sorting these samples into *glacial* and *fluvial*

110 bins, we use Sweet and Brannan's (2016) 5-point averaged fluvial-glacial (F/G) microtextural

111 ratio. Samples with a 5-point averaged F/G > 1 are classified as *fluvial* samples and samples with

112 a 5-point averaged F/G < 1 are classified as *glacial*. Kalińska-Nartiša et al. (2017) analyzed three

113 aeolian samples and two glacial samples from the Russell Glacier in southwest Greenland.

114 Finally, Smith et al. (2018) analyzed 25 fluvial and glacial samples from the Anza-Borrego

115 Desert in California, the Auster and Storelvi Rivers in Norway, the Rio Guayanés in Puerto Rico,

116 and the Rio Parón in Peru. Because Smith et al. (2018) saw no significant change in percussion

117 features along each of the river transects—even in glaciofluvial settings—the *fluvial* samples in

118 Smith et al. (2018) are defined as those collected along river transects and the *glacial* samples

119 are defined as those collected at moraines.

120

121   *Ancient Samples*

122 **Cryogenian Bråvika Member, Svalbard, Norway.** —— We analyzed two samples of

123 the Bråvika Member from a site at Buldrevågen in north-northeast Spitsbergen (Fig. 2), one at 12

124 m and another at 22 m above the base of the Bråvika Member. We will present field observations
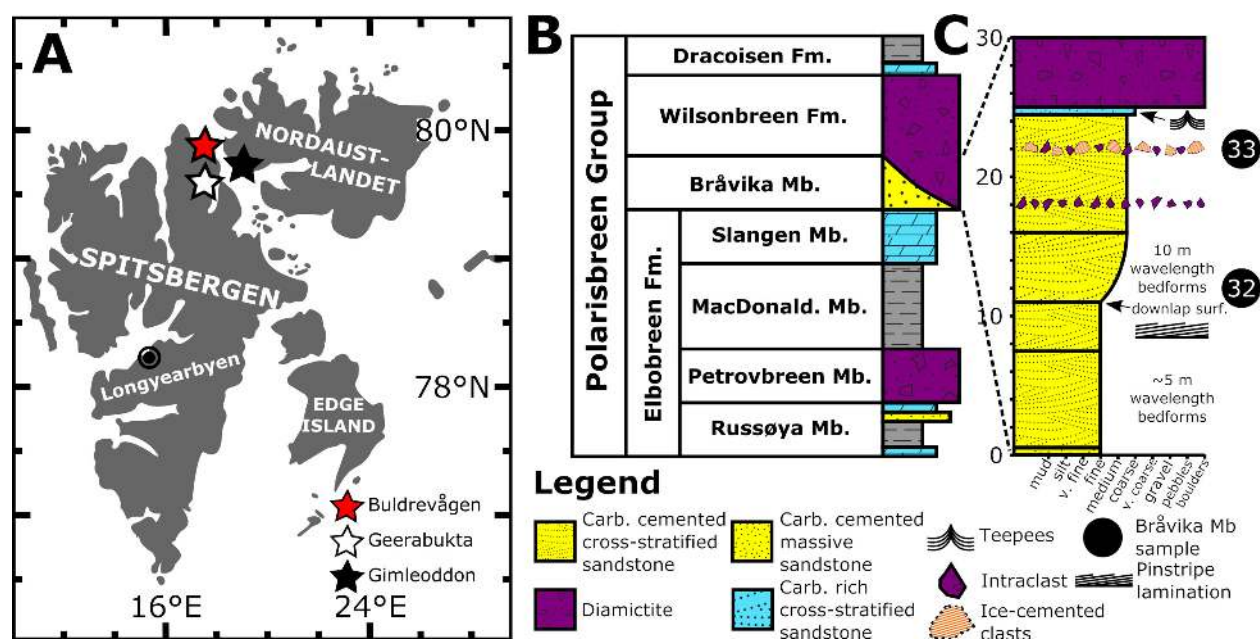
Figure 2. Geologic context and stratigraphy of the Cryogenian Bråvika Member in Svalbard. A) Map of the Svalbard archipelago. Each star indicates a site observed in this study: Buldrevågen (red), Geerabukta (white), and Gimleoddon (black). B) Generalized stratigraphic nomenclature for the Cryogenian Polarisbreen Group in Svalbard after Halverson et al. (2018). As shown here, the Bråvika Member is assigned to neither the Wilsonbreen nor the Elbobreen formations, as its assignment is a key question explored in this study. The Petrovbreen Member is correlated with the Sturtian pan-glaciation and the Wilsonbreen Formation is correlated with the Marinoan pan-glaciation (Hoffman et al. 2012). The MacDonaldryggen and Slangen members are correlated with the Cryogenian interglacial (Fairchild et al. 2016). C) Stratigraphic column of the Bråvika Member at Buldrevågen. The black circles indicate where samples 32 (J1701-156) and 33 (J1701-166) were collected for microtextural analysis.

125   of the Bråvika Member from outcrops in Buldrevågen, Geerabukta (Ny Friesland), and

126   Gimleodden (Nordaustlandet) as context for the microtextural samples.

127   The Cryogenian Bråvika Member is a northward-thickening and coarsening-upward

128   wedge of quartz arenite with lenses and beds of dolomite that outcrop in northeastern Svalbard,

129   Norway (Halverson et al. 2004). The Bråvika Member is situated between two units that are

130   interpreted to represent different Cryogenian climate states (Fig. 2). The underlying siltstone and

131   dolomite of the upper Elbobreen Formation (MacDonaldryggen and Slangen Members) are

132   correlated with the warm Cryogenian interglacial period (Fairchild et al. 2016), which spanned

133   from the Sturtian deglaciation to the Marinoan glacial initiation. Absolute age constraints on this

134   period are limited, but the Sturtian deglaciation is constrained between >662.7 ± 6.2 Ma (U-Pb

135   SIMS in South China; Yu et al. 2017) to >657.2 ± 2.4 Ma (Re-Os in Southern Australia; Kendall

136   et al. 2006), and the Marinoan glacial onset is constrained between <654.6 ± 3.8 Ma (U-Pb SIMS

137   in South China; Zhang et al. 2008) to >639.29 ± 0.26/0.31/0.75 Ma (U-Pb CA-ID-TIMS in

138   Congo; Prave et al. 2016). The overlying glacial diamictites of the Wilsonbreen Formation share

139   a reciprocal thickness relationship with the Bråvika Member and are correlated with the

140   Marinoan glaciation (Hoffman et al. 2012), which ended between 636.41 ± 0.45 Ma (U-Pb CA-

141   ID-TIMS in Southern Australia; Calver et al. 2013) and 635.2 ± 0.6 Ma (U-Pb zircon in South

142   China; Condon et al. 2005).

143   **Ancient Literature Samples.** —— In addition to the two Bråvika Member samples, we

144   compiled a set of ancient aeolian, fluvial, and glacial microtextural samples from 4 studies:

145   Mahaney and Kalm (1995), Mahaney et al. (2001), Deane (2010), and Nartišs and Kalińska-

146   Nartiša (2017) (Fig. 1; Table 2).

147   Mahaney and Kalm (1995) analyzed 23 glacial samples from the Pleistocene Dainava,

148   Ugandi, Varduva, and Latvia Tills in Estonia. Mahaney et al. (2001), following Mahaney and

149   Kalm (2000), used quantitative microtextural analysis and Eucledian distances to characterize 29

150   Pleistocene glacial samples, 3 Pleistocene glaciofluvial samples, and 21 Middle Devonian fluvial

151   samples from Estonia. All of these samples were previously collected and analyzed in Mahaney

152   and Kalm (2000). Deane (2010) compared 9 Last Glacial Maximum (LGM) glaciogenic samples

153   from Costa Rica with 9 potentially-glaciogenic samples from the Dominican Republic and found

154   that the two sample sets were statistically indistinguishable, supporting a glaciogenic history for

Table 2. List of the samples from ancient depositional environments considered in this study. Each group of samples is assigned a number for reference in Figures 1, 2, and 6 (Column #). Column S indicates the number of samples in each sample group, and column N indicates the number of quartz grains in each sample group.

Study	#	Sample	Transport	S	N	GPS Point	Geologic Period
This Study	32	Bråvika Mbr. – Buldrevågen (J1701-156)	Unknown	1	39	79°59'29"N, 17°31'20"E	Cryogenian
	33	Bråvika Mbr. – Buldrevågen (J1701-166)	Unknown	1	40	79°59'29"N, 17°31'20"E	
Nartišs and Kalińska-Nartiša (2017)	34	Middle Gauja Lowland, Latvia (Mielupīte 1.3)	Aeolian	1	16	57°30'00"N, 26°00'00"E	Pleistocene
	35	Middle Gauja Lowland, Latvia (Mielupīte 1.7)	Aeolian	1	18	57°30'00"N, 26°00'00"E	
Deane (2010)	36	Till, Costa Rica (Sample 2)	Glacial	1	300	09°29'35"N, 83°29'07"W	Pleistocene
	37	Till, Costa Rica (Sample 3)	Glacial	1	100	09°29'35"N, 83°29'07"W	
	38	Till, Costa Rica (Sample 4)	Glacial	1	100	09°29'35"N, 83°29'07"W	
	39	Till, Costa Rica (Sample 5)	Glacial	1	100	09°29'35"N, 83°29'07"W	
	40	Till, Costa Rica (Sample 8)	Glacial	1	100	09°29'35"N, 83°29'07"W	
	41	Till, Dominican Republic (Sample 10)	Glacial	1	100	19°02'01"N, 71°04'22"W	
	42	Till, Dominican Republic (Sample 11)	Glacial	1	100	19°01'60"N, 71°04'26"W	
	43	Till, Dominican Republic (Sample 17)	Glacial	1	100	19°02'07"N, 71°04'38"W	
	44	Till, Dominican Republic (Sample 18)	Glacial	1	100	19°01'39"N, 71°02'30"W	
Mahaney et al. (2001)	45	Arküla Stage Sandstone, Estonia	Fluvial	21	420	58°15'00"N, 26°30'00"E	Middle Devonian
	46	Glaciofluvial Sand, Estonia	Fluvial	3	60	58°15'00"N, 26°30'00"E	Pleistocene
	47	Till, Estonia	Glacial	29	580	58°15'00"N, 26°30'00"E	
Mahaney and Kalm (1995)	48	Latvia Till, Estonia	Glacial	5	100	58°13'28"N, 26°25'16"E	Pleistocene
	49	Varduva Till, Estonia	Glacial	5	100	58°13'28"N, 26°25'16"E	
	50	Upper Ugandi Till, Estonia	Glacial	5	100	58°13'28"N, 26°25'16"E	
	51	Lower Ugandi Till, Estonia	Glacial	5	100	58°13'28"N, 26°25'16"E	
	52	Upper Dainava Till, Estonia	Glacial	3	60	58°13'28"N, 26°25'16"E	

155   the samples from the Dominican Republic. In our study, we include samples from Deane (2010)

156   that were collected directly from known or hypothesized glacial diamicts and moraines in Costa

157   Rica and the Dominican Republic; we did not include samples from glaciolacustrine

158   environments and debris-flows. Nartišs and Kalińska-Nartiša (2017) analyzed two aeolian

159   samples from periglacial aeolian dunes associated with the retreat of the Fennoscandian ice sheet

160   after the LGM in Latvia.

161

162   **METHODS**

163   *Field Work and Sample Collecting*

164   Samples analyzed for the first time in this study were collected over multiple field

165   seasons using a variety of methods. The samples from the McMurdo Dry Valleys were originally

166   collected as microbial mats using the methods described in Mackey et al. (2015), Jungblut et al.

167   (2016), and Mackey et al. (2017). Samples from the Algodones Dunes and Waynoka Dunes were

168   collected using the methods described in Adams and Soreghan (2020). On the Juneau Icefield,

169   four sand samples of ~50 g each were collected in August 2019 from glacial moraines and an

170   ephemeral glaciofluvial melt stream on the Llewellyn Glacier (Camp 26) nunatak. Field work on

171   the Bråvika Member in Buldrevågen, Geerabukta, and Gimleodden was performed in 2017.

172

173   *Microtextural Sample Disaggregation and SEM Preparation*

174   Most samples collected for this study were unconsolidated sediment, but consolidated

175   samples were disaggregated before analysis. Both dolomite-cemented Bråvika Member samples

176   from Svalbard were disaggregated using 1N hydrochloric acid (HCl) at 50°C for 24 hours. Sand

177   samples from Lake Joyce, Lake Fryxell, and Lake Vanda were disaggregated from the microbial

178   mats using 30% hydrogen peroxide (H_2O_2) solution at 50°C for 24 hours to remove organics and

179   1N HCl at 50°C for 24 hours to remove carbonate.

180   All of the samples were then prepared for blind microtextural analysis in the style of

181   Smith et al. (2018). Samples were distributed into vials and given unique codes unknown to the

Confidential manuscript submitted to the Journal of Sedimentary Research (JSR)

182   primary researcher. These blinded conditions were maintained until after each sample's

183   microtextural data were collected.

184   After sample randomization, each sample was gently wet sieved into a 125 μm – 1 mm

185   grain size fraction and dried in an oven. After drying, the samples were treated with 30% H_2O_2

186   solution at 50°C for 24 hours to remove organics. Samples were then treated with 1N HCl

187   solution for 24 hours at 50°C to remove any remaining carbonate coatings. Neither H_2O_2 nor

188   low-concentration HCl at these temperatures and time frames affects quartz microtextures (Pye

189   1983; Keiser et al. 2015; Smith et al. 2018).

190   Samples were then treated using the citrate-bicarbonate-dithionite (CBD) method

191   (Janitsky 1986) to remove iron-oxide and manganese-oxide coatings. Between all chemical

192   treatments, the samples were thoroughly rinsed and dried. These samples were not sonicated to

193   prevent artificially inducing microtextures (Porter 1962).

194   Following these treatments, 50 grains that appeared to be quartz (e.g. translucent, no

195   obvious cleavage, etc.) were randomly selected from each sample for microtextural analysis

196   using a reflected-light microscope. The selected grains were mounted on an aluminum SEM stub

197   with double-sided carbon tape in a 10x5 grid and then coated with a 5 nm thick platinum-

198   palladium alloy (Pt/Pd; 80/20) sputter coating to prevent charging under the SEM. Although a

199   gold (Au) or gold-palladium alloy (Au/Pd) coating is frequently used for SEM samples (Vos et

200   al. 2014), Pt/Pd is a better alternative to Au coatings because Pt/Pd coatings have a smaller grain

201   size that allows for higher-resolution analysis (5-10 nm Au vs. 4-8 nm Au/Pd vs. 2-3 nm Pt/Pd;

202   Goldstein et al. 1992).

203

204   *SEM Imaging and Analysis*

13

205   All grains in each sample were photographed at a 30° tilt on a Zeiss FESEM Supra55VP

206   using a secondary electron (SE2) detector at 20 kV EHT. Viewing the grains at a 30° angle helps

207   to identify smaller microtextures that are difficult to identify at a 0° angle (Margolis and Krinsley

208   1971). During imaging, energy-dispersive spectroscopy (EDS) was used to confirm the

209   composition of each quartz grain.

210   After imaging, each quartz grain was analyzed for the presence or absence of 20

211   microtextures (Fig. 3) according to the methods of Mahaney et al. (2001) and Mahaney (2002).

212   The microtextures are grouped into five bins as defined by Sweet and Soreghan (2010) that

213   differentiate features by formation process: polygenetic, percussion, high-stress, chemical, and

214   grain relief. The following formation descriptions are from Sweet and Soreghan (2010).

215   Polygenetic features are formed through a variety of processes. Percussion features are formed

216   via grain saltation. High-stress features are formed when grains are subjected to high shear

217   stresses. Chemical features are formed via silica dissolution or precipitation. Grain relief refers to

218   the difference between the high and low points on the grain surface.

219   Grains with extreme diagenetic overprint (e.g. $\geq$ ~90% estimated coverage of diagenetic

220   overprint; Fig. S2) were removed from the sample dataset. The probability of occurrence for

221   each microtexture p_m was calculated by dividing the sum of the counts for a given microtexture

222   by the total number of grains in the sample (Smith et al. 2018).

223   Previous microtextural studies have used a range of sample sizes, from less than 20

224   grains per sample (Krinsley and Funnell 1965; Coch and Krinsley 1971; Blackwelder and Pilkey

225   1972) to 100 grains or more per sample (Vincent 1976; Setlow 1978; Deane 2010). This study

226   analyzed $\leq$ 50 grains per sample as a midpoint between these. However, non-quartz grains and

227   diagenetically overprinted grains were removed from the sample dataset, making 50 grains the
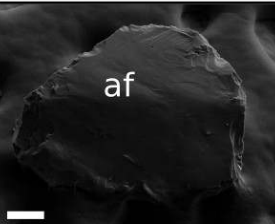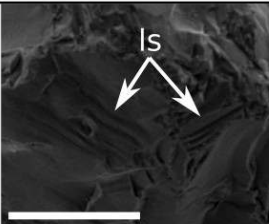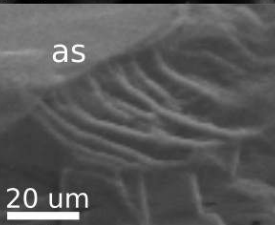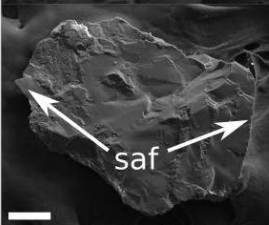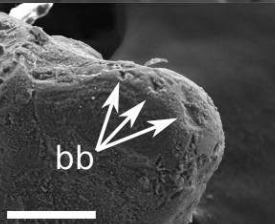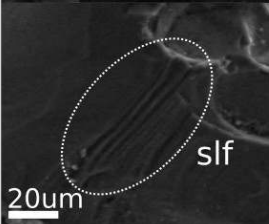
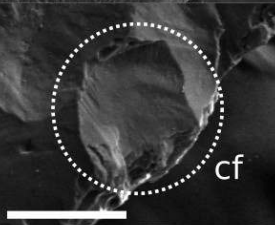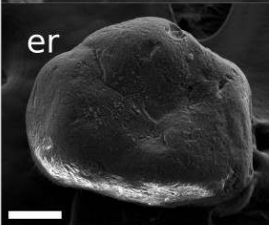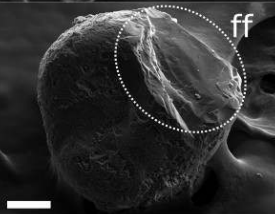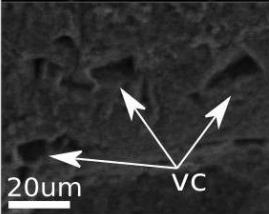| Microtexture	Abbr.	Description	Formation Process	Example Photo	Microtexture	Abbr.	Description	Formation Process	Example Photo
Abrasion Features	af	Rubbed or worn surface	Polygenetic		Linear Steps	ls	Widely spaced linear features, typically > 5 µm apart	Polygenetic	
Arc-Shaped Steps	as	Deep tears or breaks caused by impact; Several microns deep and typically spaced > 5 µm apart	Polygenetic		Sharp Angular Features	saf	Distinct sharp edges on grain surface	Polygenetic	
Breakage Blocks	bb	Blocky void marking removal of material, typically along an edge	Polygenetic		Subparallel Linear Fractures	slf	Linear fractures, typically < 5 µm spacing	Polygenetic	
Conchoidal Fractures	cf	Smooth, curved fracture	Polygenetic		Edge Rounding	er	Rounded edges on grains	Percussion	
Fracture Faces	ff	Smooth and clean fractures	Polygenetic		V-Shaped Percussion Cracks	vc	V-shaped fractures or indentions with typical sizes ranging from 1 µm to 30 µm	Percussion	

Figure 3A. Photos and description of microtextures used in this study. Scale bars are 100 µm unless otherwise noted.

Confidential manuscript submitted to the Journal of Sedimentary Research (JSR)
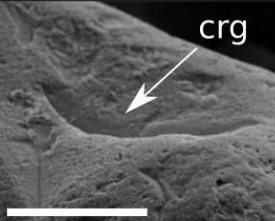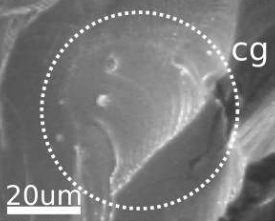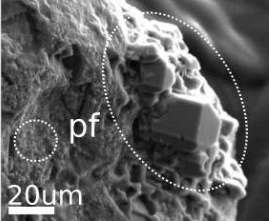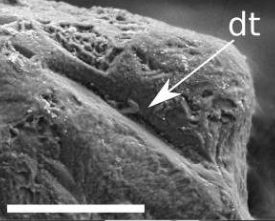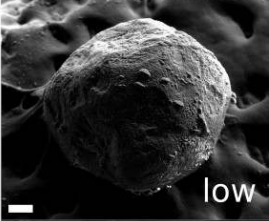
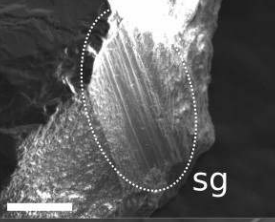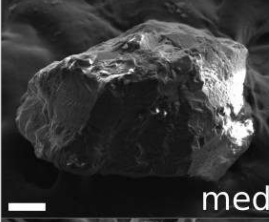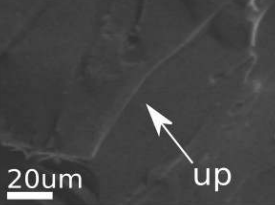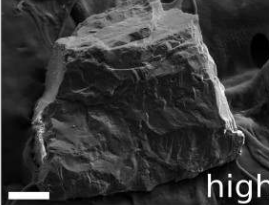| Microtexture	Abbr.	Description	Formation Process	Example Photo	Microtexture	Abbr.	Description	Formation Process	Example Photo
Crescentic Gouges	crg	Crescent-shaped gouges with convex and concave limbs that have depths > 5 μm	High-Stress		Dissolution Etching	de	Cavities from chemical dissolution; often crystallo-graphically oriented	Chemical	
Curved Grooves	cg	Curved abrasion feature caused by sustained high-stress contact with another grain, < 5 μm deep	High-Stress		Precipitation Features	pf	Coatings of amorphous silica precipitation	Chemical	
Deep Troughs	dt	Grooves > 10 μm deep	High-Stress		Low Relief	low	Nearly smooth surface without topographic irregularities	Entire history of grain	
Straight Grooves	sg	Linear grooves < 10 μm deep	High-Stress		Medium Relief	med	Semi-smooth surface with topographic irregularities	Entire history of grain	
Upturned Plates	up	Surfaces of impact where plates of variable size are partiallly torn from surface, typically > 5 μm	High-Stress		High Relief	high	Topographically irregular surface with pronounced swells and swales	Entire history of grain	

Figure 3B. Photos and description of microtextures used in this study. Scale bars are 100 μm unless otherwise noted.

16

228   upper limit for samples in this study. To address this, samples with ≥ 15 eligible quartz grains

229   were considered statistically significant for analysis; samples with < 15 eligible quartz grains

230   were not analyzed. This limit of 15 grains was selected because it is the midpoint of the lower

231   limit recommended sample sizes of Costa et al. (2012), who advocated for a median number of

232   20 grains per sample, and of Vos et al. (2014), who advocated for a lower limit of 10 grains per

233   sample.

234

235   *Principal Component Analysis (PCA)*

236   We performed PCA on the modern and ancient suites of microtextural data using Scikit-

237   learn 0.21.2 (Pedregosa et al. 2011). This ordination excluded microtextures that were not

238   analyzed by all authors, leaving 12 microtextures that were analyzed by every author in the

239   dataset. These microtextures were arc-shaped steps, conchoidal fractures, linear steps, sharp

240   angular features, subparallel linear fractures, edge rounding, v-shaped percussion cracks, curved

241   grooves, precipitated features, low relief, medium relief, and high relief (Fig. 3; Tables S1–S2).

242   The principal component axes are first derived from the modern suite of microtextural

243   data and then the ancient samples are fitted to these new axes. These axes are shown in three

244   biplots: PC1 vs. PC2; PC1 vs. PC3; and PC2 vs. PC3. In each biplot, 95% confidence ellipses

245   centered at the mean were calculated for each modern transport mode using the methods of

246   Schelp (2019). The broken-stick criterion (Frontier 1976; Jackson 1993; Legendre and Legendre

247   1998; Peres-Neto et al. 2003) was used to determine the significance of the microtextural

248   loadings.

249

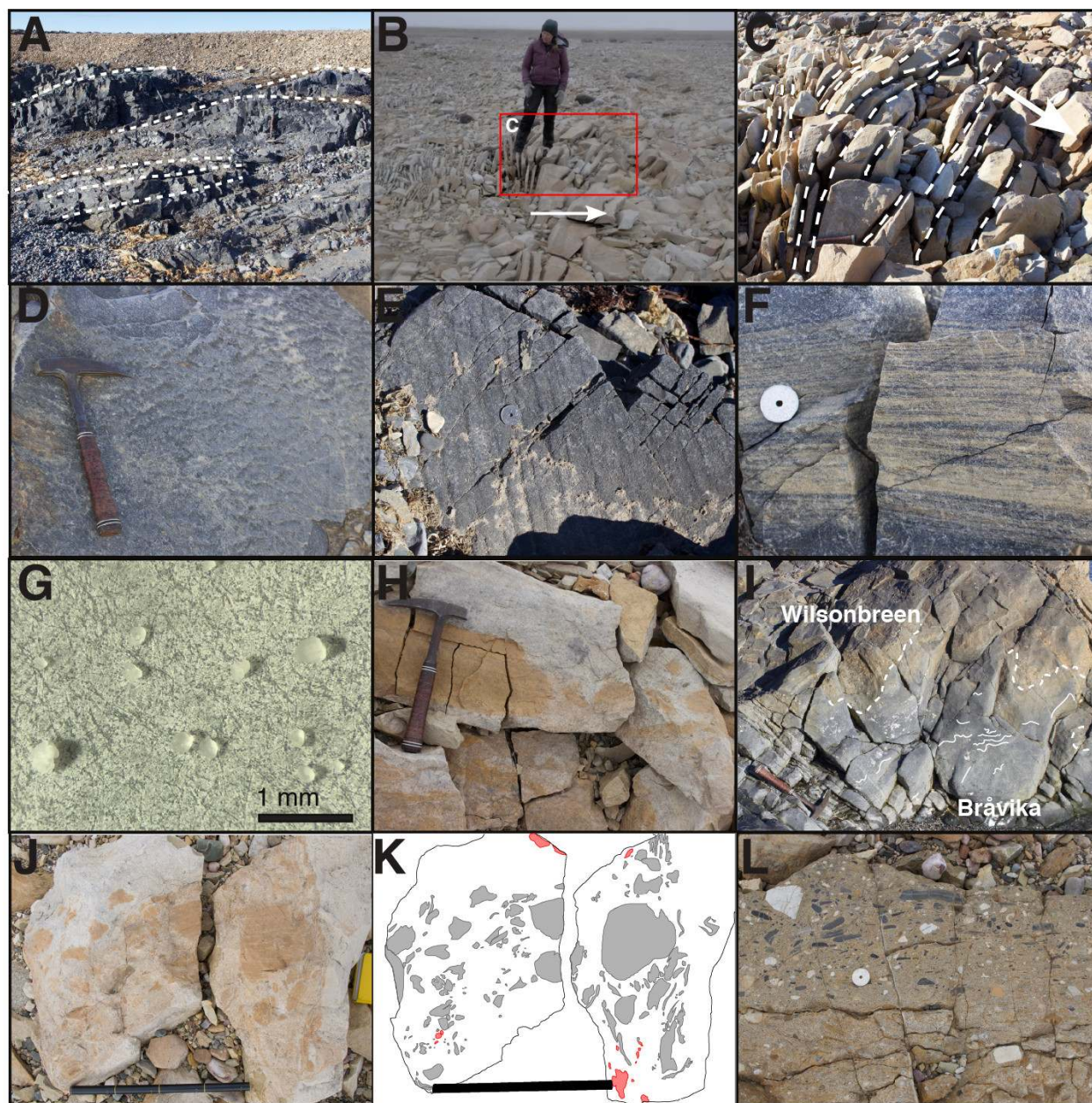250   **RESULTS**

17

Figure 4. Field observations of the Bråvika Member and related units. All field photographs are of the Bråvika Member and are credited to K.D. Bergmann unless otherwise noted. A) Annotated photograph of large-scale bedforms exposed at Gimleodden. Dashed lines trace bedding surfaces. Hammer for scale. B) Photograph of frost-shattered trough crossbedding at 12 m in Buldrevågen (Fig. 2C), where the fracture planes are bedding surfaces. Arrow points upsection. The box highlights the location of C) (Photo credit: A.B. Jost). C) Annotated close-up of trough crossbedding. The dashed lines trace bedding surfaces and the arrow points upsection. D) Adhesion ripples on a bedding plane at Geerabukta. E) Potential adhesion ripples on a bedding plane at Gimleodden. F) Pinstripe lamination at Geerabukta. G) Photomicrograph of frosted grains from the Bråvika Member at Buldrevågen after dissolution of the dolomite cement with

18

acid (Photo credit: J.N. Reahl). H) Close-up of sand intraclasts with diffuse edges at Buldrevågen. I) Soft sediment deformation in the upper Bråvika Member under the Wilsonbreen tillite at Gimleodden, consistent with deformation of unlithified Bråvika sand by overriding ice. Dashed line marks the diffuse contact between the two units and solid lines trace contorted, folded beds within the Bråvika Member. Hammer for scale. J) Sandstone intraclasts with diffuse boundaries and greenish tan, pebbly, coarse sandstone intraclasts at 22 m in Buldrevågen (Fig. 2C). Bar is 40 cm long. K) Line drawing of J at the same scale; sandstone intraclasts are shaded gray, and greenish tan pebbly, coarse sandstone intraclasts are shaded red. L) The Wilsonbreen Formation at Buldrevågen, pictured here, has a greenish tan pebbly sandstone matrix.

251   *Bråvika Member Field Observations*

252   Field observations of the Bråvika Member in Buldrevågen (79°59'29"N, 17°31'20"E),

253   Geerabukta (79°38'06"N, 17°43'48"E), and Gimleodden (79°48'19"N, 18°24'04"E) show

254   evidence of bedforms with 5-10 m wavelength and 1-3 m amplitude, trough cross-bedding,

255   adhesion ripples, pinstripe lamination (at 9 m in Fig. 2C) and grains that are frosted, well-

256   rounded, and well-sorted (Fig. 4A-G). At the Gimleodden site, there is also evidence of soft

257   sediment deformation in the Bråvika Member at the contact with the Wilsonbreen Formation

258   (Fig. 4I). At the Buldrevågen site, the Bråvika Member hosts sandstone intraclasts with diffuse

259   boundaries and no obvious cements at 22 m above the base of the Bråvika Member, as well as

260   pebbly sandstone intraclast conglomerates at 18 m and 22 m (7 m and 3 m below the

261   Wilsonbreen Formation contact, respectively; Figs. 2C, 4J-K). The pebbly sandstone intraclast

262   conglomerate is similar in color to the overlying Wilsonbreen Formation (Fig. 4L).

263

264   *Microtextural Dataset Description*

265   This microtextural dataset is composed of 113 data points from modern and ancient

266   aeolian, fluvial, and glacial settings. 92 of these data points come from modern settings and 21

267   come from ancient settings. The data are compiled from 10 studies: this study (10% of the total

268   datapoints), Smith et al. (2018) (22%), Kalińska-Nartiša et al. (2017) (4%), Nartišs and Kalińska-

269   Nartiša (2017) (2%), Sweet and Brannan (2016) (35%), Stevic (2015) (2%), Deane (2010) (8%),

270   Mahaney et al. (2001) (3%), Mahaney et al. (1996) (10%), and Mahaney and Kalm (1995) (4%).

271   Most data points in this analysis represent a single sample of N grains. The data points from

272   Mahaney and Kalm (1995) and Mahaney et al. (2001) are instead the published averages of

273   larger sets of unavailable raw data from each study.

274   Within the modern samples, 10% of the samples are aeolian, 45% are fluvial, and 45%

275   are glacial. 60% of the modern aeolian samples come from periglacial settings and 73% of the

276   modern fluvial samples come from glaciofluvial settings. All of the modern glacial samples

277   come from active glacial environments. Within the ancient samples, 90% are constrained to

278   particular depositional environments: 10% of the samples are aeolian, 10% are fluvial, and 71%

279   are glacial. The remaining 10% of the ancient samples are from the Cryogenian Bråvika

280   Member, and determining their depositional setting is a goal of this study.

281

282   *Probability of Occurrence*

283   **Modern Samples.** —— Modern aeolian samples are the most likely to have edge

284   rounding (0.90 avg.), precipitated features (0.59 avg.), and low relief (0.31 avg.) compared to

285   modern fluvial and glacial samples, which in turn are more likely to have high relief (0.40 fluvial

286   avg.; 0.36 glacial avg.) and subparallel linear fractures (0.63 fluvial avg.; 0.50 glacial avg.) (Fig.

287   5). These transport modes also share similar probabilities of occurrence for some features.

288   Glacial and aeolian samples share similar probabilities of curved grooves (0.33 glacial avg., 0.27

289   aeolian avg.) compared to fluvial samples. Fluvial and aeolian samples also share similar

290   probabilities of v-shaped percussion cracks (0.45 fluvial avg., 0.48 aeolian avg.) compared to

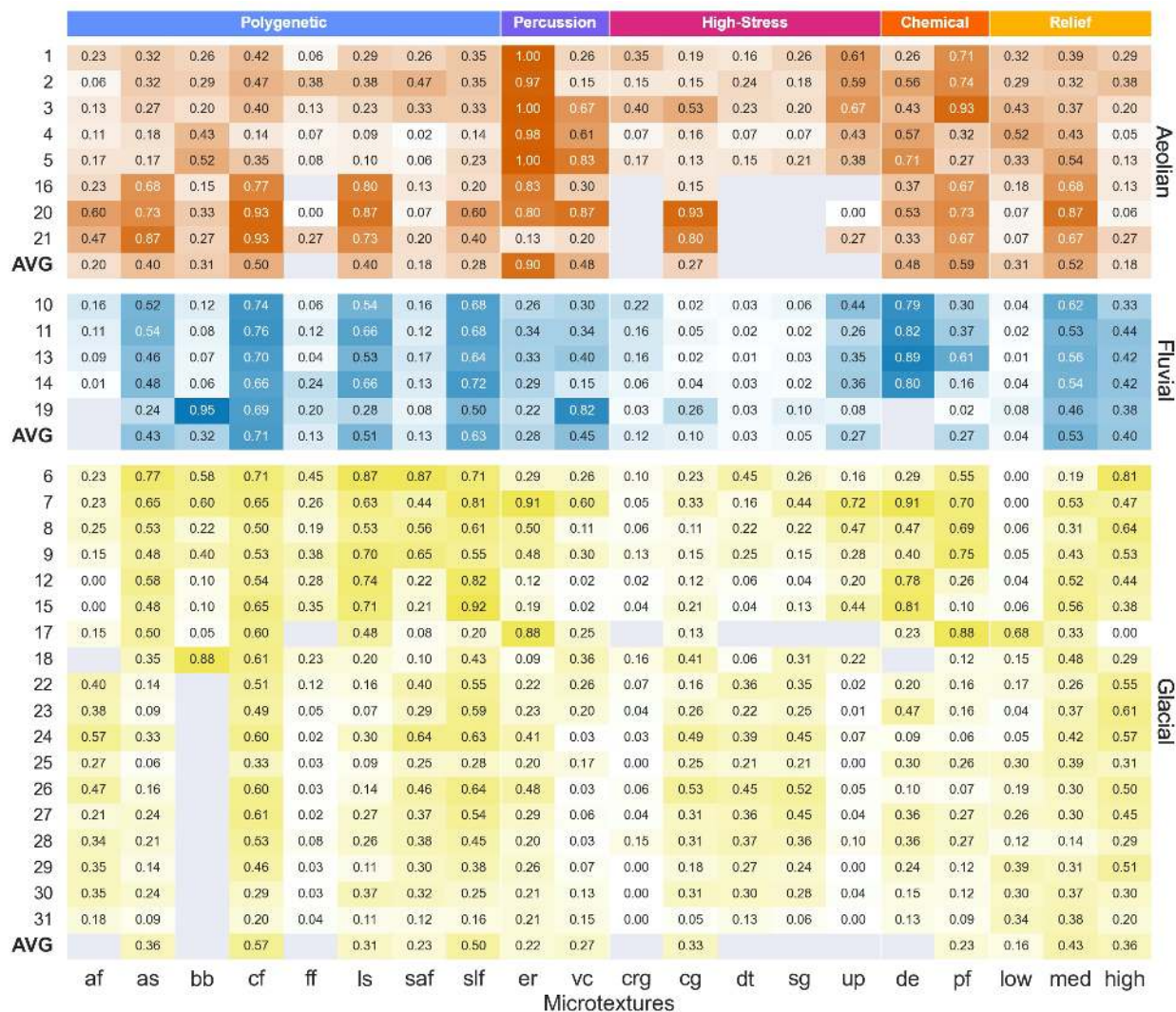Confidential manuscript submitted to the Journal of Sedimentary Research (JSR)

Figure 5. Heatmap of the microtextural probabilities of occurrence from 0 to 1 for each modern sample group used in the analysis. Samples are binned into aeolian, fluvial, and glacial transport modes. Refer to Table 1 for sample group numbers and descriptions. Data are averaged for sample groups that contain more than one sample (S > 1). Refer to Figure 3A and B for microtextural abbreviations. The average of each transport mode for the modern samples (AVG) is at the bottom of each bin. Microtextures that were not analyzed within a study are grayed out.

291   glacial samples. The probability of occurrence of arc-shaped steps, conchoidal fractures, linear

292   steps, sharp angular features, and medium relief are not substantially different between the three

293   transport modes.

21

294   Study-specific variations in microtextural probabilities occur within each transport mode.

295   In the aeolian transport mode, samples from Stevic (2015) (samples 20–21; Table 1) are more

296   likely to have curved grooves (0.80–0.93) compared to other aeolian samples in the dataset

297   (0.13–0.19). The fluvial grains from Sweet and Brannan (2016) (sample 19) are more likely to

298   have v-shaped percussion cracks (0.82) compared to the remaining fluvial samples from Smith et

299   al. (2018) (0.15–0.40). Glacial grains from this study (samples 6–9) and Kalińska-Nartiša et al.

300   (2017) (sample 17) have the highest probabilities of edge rounding (0.29–0.91) and precipitated

301   features (0.55–0.88) compared to the remaining glacial samples. The glacial grains from

302   Kalińska-Nartiša et al. (2017) are also the most likely to have low relief (0.68).

303   **Ancient Samples. ——** Both samples from the Cryogenian Bråvika Member (samples 32–

304   33; Table 2) have high probabilities of edge rounding (1.00), precipitated features (1.00), and

305   upturned plates (0.85–0.97; Fig. 6). Pleistocene aeolian sand samples from Nartišs and Kalińska-

306   Nartiša (2017) (samples 34–35) have high abundances of edge rounding, dissolution etching, and

307   precipitated features (all categorized as "abundant"; >0.75 probability of occurrence). Grains

308   from the middle Devonian Arküla Stage fluvial sand samples (sample 45) and Pleistocene

309   glaciofluvial sand samples (sample 46) from Estonia (Mahaney et al. 2001) are more likely to

310   have edge rounding (0.56–0.64), v-shaped percussion cracks (0.53–0.61), and low relief (0.35–

311   0.59) compared to grains from the modern fluvial average. The fluvial samples from Mahaney et

312   al. (2001) also have lower probabilities of arc-shaped steps (0.00–0.23), conchoidal fractures

313   (0.06–0.39), linear steps (0.00–0.26), subparallel linear fractures (0.08–0.35), upturned plates

314   (0.00–0.04), and high relief (0.05–0.18) compared to the modern fluvial average. Grains from the

315   Pleistocene tills in Costa Rica and the Dominican Republic (samples 36-44; Deane 2010) are

316   more likely to have subparallel linear fractures (0.86-0.96) and medium relief (0.60-0.76)
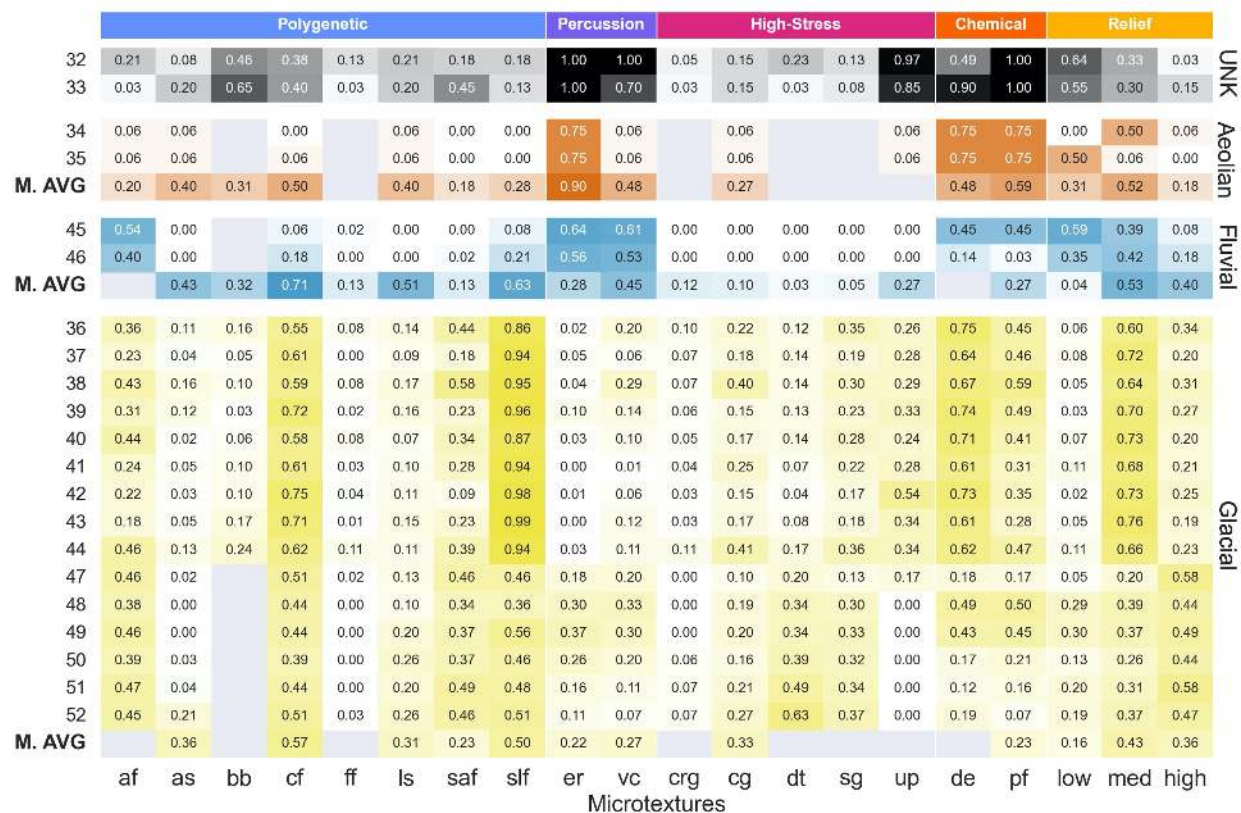
Figure 6. Heatmap of the microtextural probabilities of occurrence from 0 to 1 for each ancient sample group used in the analysis. Samples are binned into "unknown" (UNK; Bråvika Member), aeolian, fluvial, and glacial transport modes. Refer to Table 2 for sample group numbers and descriptions. Data are averaged for sample groups that contain more than one sample (S > 1). Refer to Figure 3A and B for microtextural abbreviations. The average of each transport mode for the modern samples (M. AVG) from Figure 5 is at the bottom of each bin. Microtextures that were not analyzed within a study are grayed out.

317   compared to the modern glacial average. The Pleistocene tills from Mahaney et al. (2001)

318   (sample 47) and Mahaney and Kalm (1995) (samples 48-52) are broadly comparable to the

319   modern glacial average.

320

321   *Principal Component Analysis*

322   Within the PCA ordination, the PC1, PC2, and PC3 axes capture about 66% of the

323   variance in the modern dataset (27.01%, 21.33%, and 17.43%, respectively). Along the PC1 axis
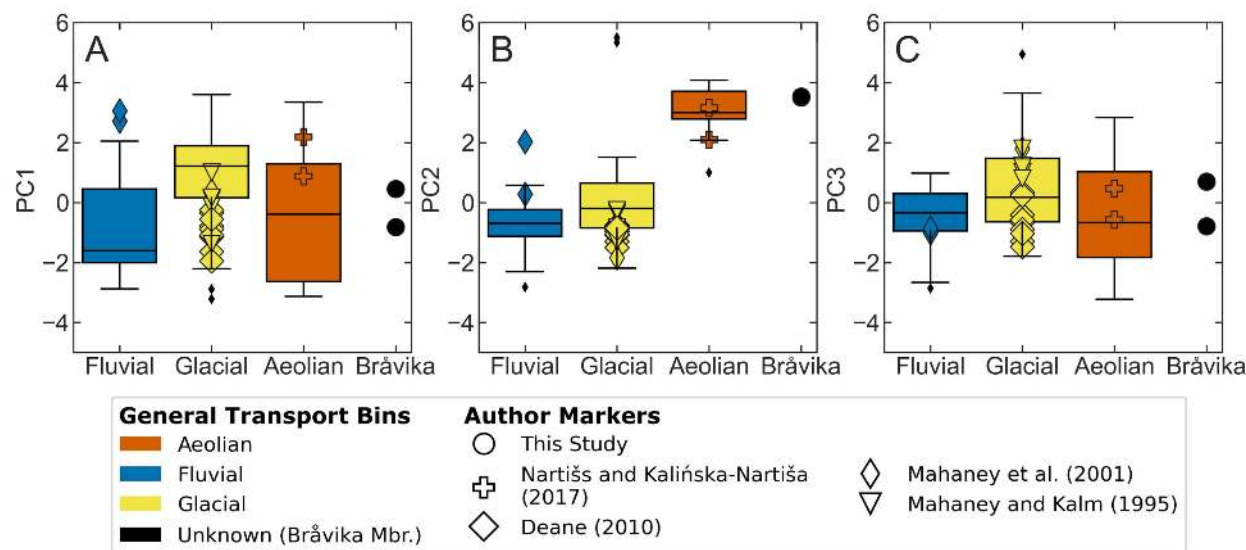
23

Confidential manuscript submitted to the Journal of Sedimentary Research (JSR)

Figure 7. Boxplots of the modern aeolian, fluvial, and glacial samples along the PC1 (A), PC2 (B), and PC3 (C) axes. The small black diamonds represent modern outliers for each transport mode. The ancient samples are plotted as individual points over the boxplots.

324   (Figs. 7–8; Table S3), the aeolian, fluvial, and glacial samples are distributed along both sides of

325   the axis with no clear separation. However, the samples are generally separated by study along

326   PC1: the samples from Stevic (2015) and Smith et al. (2018) are distributed between -2.9 and -

327   1.1 and the samples from Mahaney et al. (1996) and Sweet and Brannan (2016) are distributed

328   between -0.2 and 3.5. The samples from this study and Kalińska-Nartiša et al. (2017) are widely

329   distributed on PC1, where the samples from this study are distributed between -3.2 to 3.3 and the

330   Kalińska-Nartiša et al. (2017) samples are distributed between -3.1 and 1.7. The sample

331   separation along PC1 is predominantly driven by the abundance of linear steps and arc-shaped

332   steps, which have the largest (-0.489) and second largest (-0.425) negative loadings along PC1

333   (Table 3). However, neither of these loadings are strongly associated with PC1 according to the

334   broken-stick criterion.

335   Along the PC2 axis, modern aeolian samples are distinctly separated from modern glacial

336   and fluvial samples. This separation between aeolian and fluvial/glacial samples along PC2 is
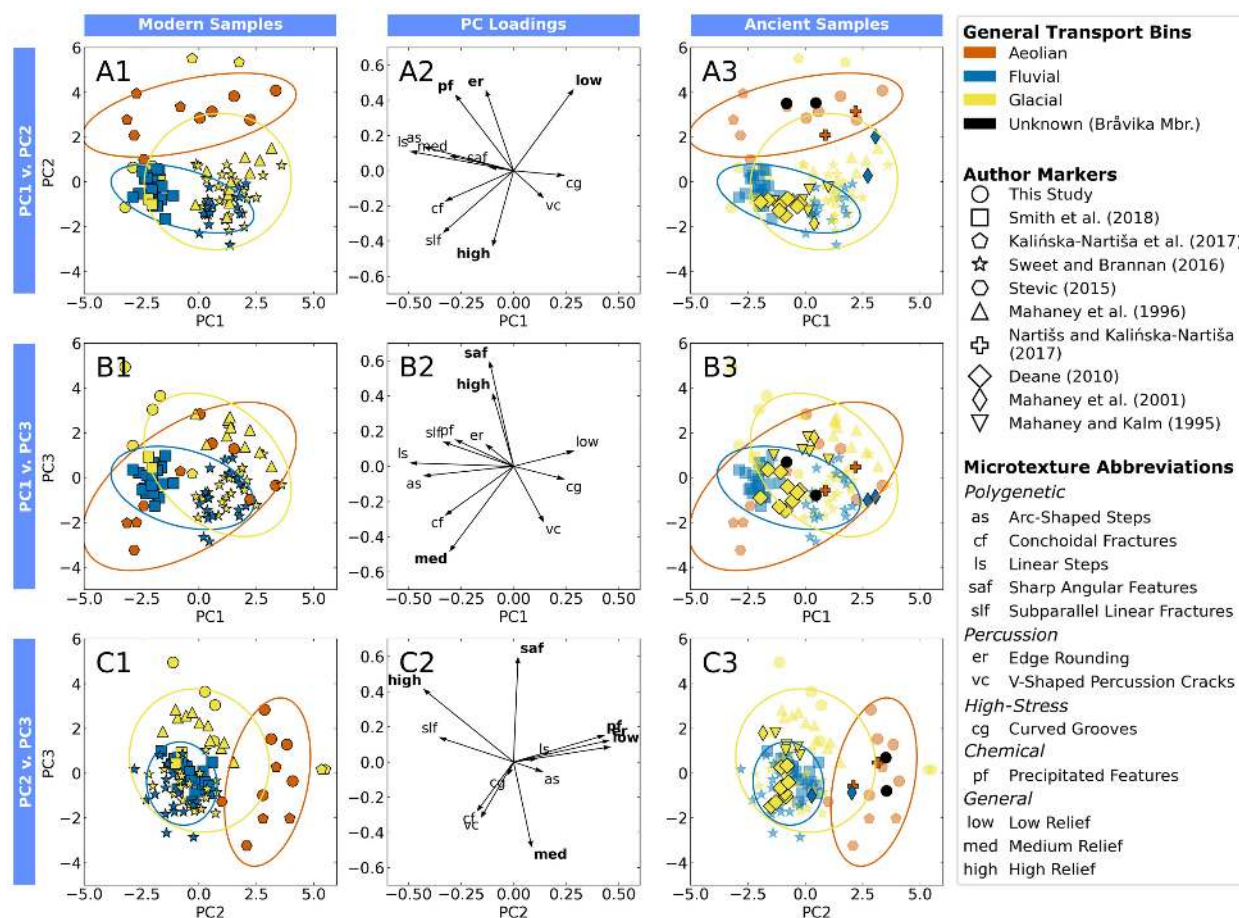
Figure 8. PCA ordination using all 12 microtextures analyzed by all studies. Each row is a biplot in A) PC1-PC2 space; B) PC1-PC3 space; and C) PC2-PC3 space. Column 1 plots the modern sample data within each space (this study through Mahaney et al. 1996), Column 2 plots the microtextural loadings, and Column 3 plots the ancient sample data (this study, Nartišs and Kalińska-Nartiša 2017 through Mahaney and Kalm 1995) over the existing modern reference frame. Refer to Table 3 for the loadings in Column 2. Microtextures with significant loadings in Column 2 are in bold. The ellipses are 95% confidence intervals of each modern transport mode that are centered at the mean of the transport mode in each coordinate space. The ellipses are calculated using the methods of Schelp (2019).

337   driven by low relief, edge rounding, and precipitated features in the positive direction (loadings

338   of 0.457, 0.455, and 0.432) and high relief in the negative direction (-0.427), which are all

339   associated with PC2 according to the broken-stick criterion.

340   Along the PC3 axis, the three transport modes are distributed along both sides of the axis

341   with no clear separation, similar to the distribution along PC1. However, unlike the distribution

25

Table 3. Ranked loadings and squared loadings of microtextures from the PCA ordination (Fig. 8). Refer to Figure 3A and B for microtexture abbreviations. The microtextures in bold have squared loadings that are greater than the expected value of their associated principal component according to the broken-stick criterion (Frontier 1976; Jackson 1993; Legendre and Legendre 1998; Peres-Neto et al. 2003).

PC1			PC2			PC3		
Expected PC Value:		0.259	Expected PC Value:		0.175	Expected PC Value:		0.134
Microtexture	Loading	Loading^2	Microtexture	Loading	Loading^2	Microtexture	Loading	Loading^2
low	0.286	0.082	**low**	**0.457**	**0.209**	**saf**	**0.592**	**0.351**
cg	0.239	0.057	**er**	**0.455**	**0.207**	**high**	**0.411**	**0.169**
vc	0.141	0.020	**pf**	**0.432**	**0.186**	pf	0.153	0.023
high	-0.104	0.011	as	0.139	0.019	slf	0.135	0.018
saf	-0.114	0.013	ls	0.112	0.013	er	0.126	0.016
er	-0.128	0.017	med	0.090	0.008	low	0.089	0.008
pf	-0.272	0.074	saf	0.018	0.000	ls	0.019	0.000
med	-0.300	0.090	cg	-0.028	0.001	as	-0.055	0.003
cf	-0.324	0.105	vc	-0.153	0.023	cg	-0.071	0.005
slf	-0.335	0.112	cf	-0.168	0.028	cf	-0.279	0.078
as	-0.425	0.181	slf	-0.350	0.123	vc	-0.312	0.097
ls	-0.489	0.239	**high**	**-0.427**	**0.182**	**med**	**-0.482**	**0.232**

342   along PC1, the samples are not as distinctly separated by study. The significant microtextures

343   along PC3 are sharp angular features and high relief in the positive direction (0.592 and 0.411),

344   and medium relief in the negative direction (-0.482). All of these microtextures are associated

345   with PC3 according to the broken-stick criterion.

346   Along each principal component axis, at least 89% of the ancient aeolian, fluvial, and

347   glacial samples plot within the upper and lower adjacent values of the boxplot of their modern

348   counterparts: 89% on PC1, 95% on PC2, and 100% on PC3 (Fig. 7). In each biplot (Fig. 8), at

349   least 74% of these ancient samples plot within the 95% confidence ellipses of their modern

350   counterparts: 89% in the PC1-PC2 biplot (A3), 74% in the PC1-PC3 biplot (B3), and 95% in the

351   PC2-PC3 biplot (C3). The median of the percent agreement between the ancient samples and

352   their modern counterparts is 92%.

353   The 92% median agreement between the modern and ancient samples demonstrates that

354   PCA of modern and ancient samples provides a valid framework for interpreting the fingerprint

355   of depositional environments in ancient samples with ambiguous depositional histories. In this

356   ordination, the two Bråvika Member samples with ambiguous depositional histories consistently

357   plot within the upper and lower adjacent values of the modern aeolian samples in each principal

358   component axis (Fig. 7) and the 95% confidence ellipses of the modern aeolian samples in each

359   biplot (Fig. 8). This placement suggests that the Bråvika Member samples analyzed in this study

360   have an aeolian origin.

361

362   **DISCUSSION**

363   *Interpreting the PCA Ordination*

364   PC1 separates the modern samples by author and accounts for the most variance in the

365   dataset (27.01%), indicating that author-specific microtextural variance is the largest individual

366   source of variance in the modern dataset. This result is consistent with the observation that SEM

367   operator variance exerts significant influence on the probabilities of occurrence of individual

368   microtextures (Culver et al. 1983). However, as Culver et al. (1983) observed using canonical

369   variate analysis, author variance is overall negligible in determining a sample's depositional

370   environment: the combined variance of PC2 and PC3 accounts for over a third of the variance in

371   the modern dataset (21.33% and 17.43%, respectively). The PC2 axis separates the samples into

372   aeolian and fluvial/glacial transport modes, and the PC3 axis separates the samples neither by

373   transport mode nor by study (Fig. 8).

374

375   *Which Microtextures Distinguish Transport Modes?*

Confidential manuscript submitted to the Journal of Sedimentary Research (JSR)

376   Aeolian sediment is defined by high probabilities of low relief, edge rounding, and

377   precipitated features, and fluvial and glacial sediments are defined by high probabilities of high

378   relief and subparallel linear fractures. The modern (Fig. 5) and ancient (Fig. 6) heatmaps show

379   that aeolian samples have the highest probabilities of low relief, edge rounding, and precipitated

380   features, and fluvial and glacial samples have the highest probabilities of high relief and

381   subparallel linear fractures. PC2 also separates the aeolian samples from the fluvial and glacial

382   samples using low relief, edge rounding, and precipitated features in the positive (aeolian)

383   direction and high relief in the negative (fluvial/glacial) direction (Fig. 8; Table 3). These

384   findings are consistent with previous observations of these microtextures: low relief, edge

385   rounding, and precipitated features have all previously been associated with windblown sediment

386   (Nieter and Krinsley 1976; Lindé and Mycielska-Dowgiałło 1980; Krinsley and Trusty 1985;

387   Mahaney 2002; Vos et al. 2014); high relief can occur on both fluvial and glacial sediments

388   (Mahaney 2002; Vos et al. 2014); and subparallel linear fractures are often associated with

389   glacial and glaciofluvial settings, the latter of which makes up 73% of the modern fluvial

390   samples in this study (Mahaney and Kalm 2000; Deane 2010; Immonen 2013; Vos et al. 2014;

391   Woronko 2016).

392   Although fluvial and glacial samples are microtexturally distinct from aeolian samples, it

393   is difficult to disambiguate the fluvial and glacial transport modes from each other in this dataset.

394   Features that are typically associated with glacial environments, such as arc-shaped steps,

395   conchoidal fractures, linear steps, and sharp angular features (Mahaney and Kalm 2000;

396   Mahaney 2002; Immonen 2013; Woronko 2016), had comparable probabilities across all three

397   modern transport modes, indicating that these features are not exclusively associated with glacial

398   environments (Fig. 5). Smith et al. (2018) also observed that arc-shaped steps and linear steps

399   may not be indicators of glacial transport. These results are consistent with Sweet and Soreghan

400   (2010)'s classification of these features as *polygenetic* features that are formed through a variety

401   of transport processes. Subparallel linear fractures are also associated with glacial and

402   glaciofluvial settings (Mahaney and Kalm 2000; Deane 2010; Immonen 2013; Vos et al. 2014;

403   Woronko 2016), but the modern fluvial average for subparallel linear fractures is higher than the

404   glacial average. Although glaciofluvial samples make up 73% of the modern fluvial samples, the

405   non-glacial fluvial samples (samples 10 and 13; Fig. 5) have similar probabilities of subparallel

406   linear fractures compared to glaciofluvial samples (samples 11, 14, and 19), suggesting that

407   subparallel linear fractures may not be an exclusively glacial feature. These results suggest that

408   fluvial and glacial samples may share microtextural similarities, but more studies comparing the

409   microtextural features of non-glacial fluvial, glaciofluvial, and glacial samples are needed to

410   understand the differences between these transport environments.

411   These results highlight the importance of precipitated features as a primary indicator of

412   transport instead of an exclusive product of diagenesis. If precipitated features were only an

413   indicator of post-depositional diagenesis, then the probability of precipitated features should

414   increase with age. However, all of the modern samples have some probability of having

415   precipitated features—particularly the aeolian samples—and the ancient samples do not show a

416   consistent increase in the probability of chemical features as the sediment age increases (Figs. 5–

417   6). Both of these observations point to precipitated features being a primary microtextural

418   feature. Although Sweet and Soreghan (2010) suggested that precipitated features should not be

419   counted because they can form via diagenesis and overprint a sample, our results indicate that

420   these features can also be a primary feature and should not be discounted, even in situations

421   where diagenesis is a concern.

422   Some microtextures often used in microtextural studies could not be included in this

423   analysis: abraded features, breakage blocks, crescentic gouges, fracture faces, deep troughs,

424   straight grooves, upturned plates, and dissolution etching. Many of these microtextures have

425   been previously associated with certain transport environments. Breakage blocks, straight

426   grooves, and fracture faces have been associated with glacial environments (Woronko 2016) and

427   upturned plates and dissolution etching have been associated with aeolian environments

428   (Margolis and Krinsley 1974; Mahaney 2002). For the purposes of comparing microtextural data

429   from multiple studies, we were limited to using the most often used microtextures in the

430   literature. Moving forward, it would be helpful to establish a consistent minimum set of

431   microtextures to be used in microtextural studies.

432

433   *Test Case: The Cryogenian Bråvika Member*

434   We now shift our focus to using the microtextural data, PCA, and stratigraphic

435   observations to constrain the depositional environment of the Cryogenian Bråvika Member from

436   Buldrevågen, Svalbard. Our combined field observations and microtextural data suggest that the

437   Bråvika Member includes aeolian deposition that may be time equivalent with the onset of the

438   syn-glacial Marinoan Wilsonbreen Formation.

439   The microtextural evidence point to an aeolian origin for the Bråvika Member. Both

440   samples from the Bråvika Member have particularly high occurrences of edge rounding,

441   precipitated features, and low relief (samples 32 and 33; Fig. 6), which have all been previously

442   associated with aeolian transport (Nieter and Krinsley 1976; Lindé and Mycielska-Dowgiałło

443   1980; Krinsley and Trusty 1985; Mahaney 2002; Vos et al. 2014). The Bråvika Member samples

444   also have high probabilities of upturned plates, which have been associated with grain frosting

445   (Margolis and Krinsley 1971). Compared to the modern and ancient aeolian, fluvial, and glacial

446   samples, the Bråvika Member samples are most similar to the aeolian samples, sharing similar

447   probabilities of low relief, edge rounding, and precipitated features (Fig. 6). These samples also

448   consistently plot within the upper and lower adjacent values (Fig. 7) and 95% confidence ellipse

449   (Fig. 8) of the modern aeolian samples. Because the ancient aeolian, fluvial, and glacial samples

450   are accurately matched with their modern counterparts 92% of the time when transformed into

451   modern PCA space, the PCA ordination is able to accurately plot samples with ambiguous

452   depositional histories alongside their most likely modern microtextural analogs.

453   An aeolian interpretation for the microtextural data is consistent with field observations

454   made in 2017 of the Bråvika Member in Buldrevågen, Geerabukta, and Gimleodden (Fig. 4).

455   Bedforms with 5–10 m wavelengths and 1–3 m amplitudes at the Gimleodden (Fig. 4A) and

456   Buldrevågen (Fig. 4B–C) sites are consistent with aeolian dunes in scale and style (Wilson 1972;

457   Pye and Tsoar 2009). There is also evidence of adhesion ripples on bedding planes at the

458   Geerabukta (Fig. 4D) and Gimleodden (Fig. 4E) sites. Adhesion ripples are formed when dry,

459   windblown sand is blown onto a wet surface, and these features have been previously observed

460   on ancient aeolian deposits (Kocurek and Fielder 1982). The presence of pinstripe lamination at

461   the Buldrevågen (Fig. 2C) and Geerabukta (Fig. 4F) sites are a strong indicator for aeolian

462   deposition (Fryberger and Schenk 1988). The high degree of grain rounding at this interval (Fig.

463   4G) is also characteristic of grains transported by aeolian processes (Folk 1980); subaqueous

464   transport does not typically produce such a high degree of grain rounding (Pettijohn 1957). The

465   frosted grains within these samples (Fig. 4G) are also a strong indicator of aeolian transport (Pye

466   and Tsoar 2009).

31

467   Field evidence also suggests that the aeolian strata of the Bråvika Member may be syn-

468   depositional with the Marinoan pan-glaciation as opposed to the Cryogenian interglacial. The

469   pebbly sandstone intraclast conglomerates' proximity to the contact with—and similar color and

470   texture as—the Wilsonbreen Formation (Figs. 2, 4) suggest that they are sourced from this unit.

471   These intraclasts' occurrences at 7 m and 3 m below the Wilsonbreen Formation contact (Fig.

472   2C) suggest that the Bråvika Member in Buldrevågen was syn-depositional with the Wilsonbreen

473   Formation and the Marinoan pan-glaciation. The intraclasts with diffuse boundaries and no

474   obvious cements at 22 m (Figs. 2, 4) are putative ice-cemented sand intraclasts. Ice-cemented

475   intraclasts form when water within the pore space of unconsolidated sand freezes portions of

476   sand into discrete clasts that can be transported and deformed into new orientations before the

477   cementing ice melts. Sand intraclasts are routinely identified as ice-cemented in glaciogenic

478   deposits (Browne and Naish 2003), and Runkel et al. (2010) has reported putative ice-cemented

479   sand intraclasts preserved in rocks as old as the middle to late Cambrian. The putative ice-

480   cemented intraclasts indicate that the Bråvika Member was at least unconsolidated during the

481   Marinoan pan-glaciation, and the occurrence of possible Wilsonbreen intraclasts 3 m below the

482   Wilsonbreen Formation contact (Fig. 2C) suggests that the upper Bråvika Member was syn-

483   depositional with the Marinoan glaciation. Evidence of soft sediment deformation at the contact

484   between the Bråvika Member and Wilsonbreen Formation at Gimleodden (Fig. 4I) is also

485   consistent with the upper Bråvika Member being unconsolidated during the Marinoan glaciation.

486   Integrating microtextural and field observations, we suggest that the upper Bråvika

487   Member includes aeolian deposition and may represent a syn-glacial aeolian sand sea, or erg,

488   contemporaneous with the Marinoan glaciation. This setting is akin to previously identified

489   Marinoan syn-glacial ergs in the Bakoye Formation of Mali (Deynoux et al. 1989) and the

32

490   Whyalla Sandstone (Elatina glaciation) of South Australia (Williams 1998; Rose et al. 2013;

491   Ewing et al. 2014). Hoffman and Li (2009) suggested that katabatic winds coming off of the

492   Marinoan ice sheet are the primary transport mechanism for these syn-glacial ergs. The

493   northward paleoflow direction of the Bråvika Member and the Bråvika Member's reciprocal

494   thickness relationship with the Wilsonbreen Formation (Halverson et al. 2004) may reflect this

495   transport mechanism, where a northward-advancing ice margin represented by the Wilsonbreen

496   Formation drives the Bråvika Member to the north with katabatic winds coming off of the

497   Marinoan ice sheet.

498   The microtextural samples analyzed in this study are specific to the interval in

499   Buldrevågen that is proximal to the Wilsonbreen contact. Given the wide range of possible facies

500   proposed by Halverson et al. (2004), Halverson (2011), Hoffman et al. (2012), and this study, the

501   Bråvika Member may represent multiple depositional environments across localities that capture

502   a transition from the Cryogenian interglacial to the Marinoan pan-glaciation.

503   Important questions remain about the apportionment of time within the strata that record

504   the Cryogenian interglacial in Svalbard. The absence of the pre-Marinoan Trezona negative δ^{13}C

505   excursion below the Wilsonbreen Formation has been used to suggest that the sedimentary

506   package between the Petrovbreen Member and the Wilsonbreen Formation is top-truncated

507   (Hoffman et al. 2012; Fairchild et al. 2016; Halverson et al. 2018). The locations of the hiatal

508   surfaces within the Bråvika Member remain ambiguous, and their locations are critical to

509   understanding the apportionment of time in these units and in the interglacial. Our work suggests

510   that the uppermost aeolian deposition within the Bråvika Member is continuous with the start of

511   Wilsonbreen deposition, but there may be important hiatal surfaces lower in the Bråvika

512   Member.

513

CONCLUSIONS

515   Quartz surface microtextures preserve the transport histories of modern and ancient

516 sediment. However, because workers count microtextures differently for samples from the same

517 depositional environment, the defining microtextures of certain transport modes are not well

518 constrained. We used PCA to directly compare quantitative microtextural data from modern and

519 ancient aeolian, fluvial, and glacial sediments across workers. Although differences between

520 workers are the largest sources of variance in the dataset, the PCA ordination shows that aeolian

521 samples are microtexturally distinct from fluvial and glacial samples across studies. Fluvial and

522 glacial samples are difficult to disambiguate from each other in this dataset, indicating that more

523 work needs to be done comparing fluvial, glaciofluvial, and glacial samples with each other. The

524 PCA ordination also demonstrates that ancient sediments and modern sediments have

525 quantitatively similar microtextural relationships. Therefore, PCA may be a useful tool to

526 elucidate the ambiguous transport histories of some ancient sediment grains. As a test case, we

527 used PCA to constrain the depositional environment of the ambiguous Cryogenian Bråvika

528 Member from Svalbard. This ordination, combined with field observations, indicates that the

529 Bråvika Member includes aeolian deposition, and suggests that the Bråvika Member may be

530 analogous to syn-glacial Marinoan aeolian sand seas such as the Bakoye Formation in Mali and

531 the Whyalla Sandstone in South Australia. This study demonstrates that PCA can distinguish

532 sedimentary environments across multiple studies, which in turn helps constrain the depositional

533 history of ambiguous sedimentary deposits like the Bråvika Member.

534

SUPPLEMENTARY MATERIAL

536   All supplementary materials related to this study—including detailed sample

537 descriptions, additional notes on PCA analysis, code, raw microtextural data, and SEM images—

538 are available at https://github.com/jreahl/Reahl_2020.

539

540   **LAND ACKNOWLEDGEMENT**

541   This work—from analysis to writing—was performed at institutions built on Indigenous

542 land, using samples collected from Indigenous lands. The samples analyzed for the first time in

543 this study were collected from the traditional and ancestral territories of the Cocopah (*Kwapa*),

544 Comanche (*Nʉmʉnʉʉ*), Keechi (*Ki:che:ss*), Kiowa (*[Gáui[dòñ:gyà*), Kumeyaay, Osage

545 (*Wahzhazhe*), Quechan (*Kwatsáan*), Salt River O'odham (Pima) and Piipaash (Maricopa), Taku

546 River Tlingit (*Lingít*), Tawakoni (*Tawá:kharih*), Waco (*Wí:koʔ*), and Wichita (*Kirikirʔi:s*).

547 Laboratory analysis and SEM analysis was performed on unceded Wampanoag land. Writing

548 was performed on the territories of the Abenaki, Chumash, and Wampanoag. These communities

549 occupied these territories before and after European colonization and live on this land to the

550 present day. We also acknowledge the dispossession of Indigenous land through the 1862 Morrill

551 Act, which turned parcels of land taken from tribal nations into seed money for land-grant

552 universities including the Massachusetts Institute of Technology. Although this

553 acknowledgement does not compensate for centuries of injustices, we hope it helps spur robust,

554 mutually beneficial collaboration between Indigenous communities and scientific efforts. We

555 encourage readers to engage with Indigenous communities and cultures around where they live

556 and work. The Native Land Digital database (native-land.ca) is an excellent resource to begin

557 this process. The best resources for prolonged learning are through direct conversation and

558 collaboration with Indigenous community members. Many Indigenous communities have

Confidential manuscript submitted to the Journal of Sedimentary Research (JSR)

559   dedicated cultural heritage officers who may be available as partners in these efforts; the

560   National Congress of American Indians (ncai.org) hosts a tribal directory with contact

561   information, as well as the National Association of Tribal Historic Preservation Officers

562   (nathpo.org).

563

564   **ACKNOWLEDGEMENTS**

590

AUTHOR CONTRIBUTIONS

592   J.N.R. wrote the manuscript, collected samples from the Juneau Icefield, performed SEM

593   analysis on all samples, and performed the PCA analysis. M.D.C. and K.D.B. were the primary

594   advisors to J.N.R. J.W. shared her stratigraphic columns and samples of the Bråvika Member, as

595   well as insight on statistics and machine learning. J.W., M.D.C., T.J.M., and K.D.B.

596   characterized and collected samples of the Bråvika Member in Svalbard during their 2017 field

597   season. T.J.M. contributed samples from the McMurdo Dry Valleys. All authors reviewed the

598   final manuscript.

599

REFERENCES

601   Adams, S. M., 2018, Evaluating desert silt production using field, experimental, and remote-
602   sensing methods [MS Thesis]: University of Oklahoma, 74 p.

603   Adams, S. M., and Soreghan, G. S., 2020, A test of the efficacy of sand saltation for silt
604   production: Implications for the interpretation of loess: Geology, v. 48, p. 1105–1109.

605   Blackwelder, P. L., and Pilkey, O. H., 1972, Electron microscopy of quartz grain surface
606   textures: the U.S. Eastern Atlantic continental margin: Journal of Sedimentary Petrology,
607   v. 42, p. 520–526.

608　Browne, G. H., and Naish, T. R., 2003, Facies development and sequence architecture of a late
609　　　　Quaternary fluvial-marine transition, Canterbury Plains and shelf, New Zealand:
610　　　　implications for forced regressive deposits: Sedimentary Geology, v. 158, p. 57–86.

611　Bull, P. A., 1981, Environmental reconstruction by electron microscopy: Progress in Physical
612　　　　Geography, v. 5, p. 368–397.

613　Calver, C. R., Crowley, J. L., Wingate, M. T. D., Evans, D. A. D., Raub, T. D., and Schmitz, M.
614　　　　D., 2013, Globally synchronous Marinoan deglaciation indicated by U-Pb geochronology
615　　　　of the Cottons Breccia, Tasmania, Australia: Geology, v. 41, p. 1127–1130.

616　Coch, N. K., and Krinsley, D. H., 1971, Comparison of stratigraphic and electron microscopic
617　　　　studies in Virginia Pleistocene coastal sediments: The Journal of Geology, v. 79, p. 426–
618　　　　437.

619　Condon, D., Zhu, M., Bowring, S., Wang, W., Yang, A., and Jin, Y., 2005, U-Pb Ages from the
620　　　　Neoproterozoic Doushantuo Formation, China: Science, v. 308, p. 95–98.

621　Costa, P. J. M., Andrade, C., Dawson, A. G., Mahaney, W. C., Freitas, M. C., Paris, R., and
622　　　　Taborda, R., 2012, Microtextural characteristics of quartz grains transported and
623　　　　deposited by tsunamis and storms: Sedimentary Geology, v. 275–276, p. 55–69.

624　Costa, P. J. M., Andrade, C., Mahaney, W. C., Marques da Silva, F., Freire, P., Freitas, M. C.,
625　　　　Janardo, C., Oliveira, M. A., Silva, T., and Lopes, V., 2013, Aeolian microtextures in
626　　　　silica spheres induced in a wind tunnel experiment: Comparison with aeolian quartz:
627　　　　Geomorphology, v. 180–181, p. 120–129.

628　Costa, P. J. M., Park, Y. S., Kim, Y. D., Quintela, M., Mahaney, W. C., Dourado, F., and
629　　　　Dawson, S., 2017, Imprints In Silica Grains Induced During An Open-Channel Flow
630　　　　Experiment: Determination of Microtextural Signatures During Aqueous Transport:
631　　　　Journal of Sedimentary Research, v. 87, p. 677–687.

632　Culver, S. J., Bull, P. A., Campbell, S., Shakesby, R. A., and Whalley, W. B., 1983,
633　　　　Environmental discrimination based on quartz grain surface textures: a statistical
634　　　　investigation: Sedimentology, v. 30, p. 129–136.

635　Deane, S. M., 2010, Quartz grain microtextures and sediment provenance: Using scanning
636　　　　electron microscopy to characterize tropical highland sediments from Costa Rica and the
637　　　　Dominican Republic [MS Thesis]: University of Tennessee, Knoxville, 137 p.

638　Deynoux, M., Kocurek, G., and Proust, J. N., 1989, Late Proterozoic periglacial aeolian deposits
639　　　　on the West African Platform, Taoudeni Basin, western Mali: Sedimentology, v. 36, p.
640　　　　531–549.

641　Ewing, R. C., Eisenman, I., Lamb, M. P., Poppick, L., Maloof, A. C., and Fischer, W. W., 2014,
642　　　　New constraints on equatorial temperatures during a Late Neoproterozoic snowball Earth
643　　　　glaciation: Earth and Planetary Science Letters, v. 406, p. 110–122.

644 Fairchild, I. J., Fleming, E. J., Bao, H., Benn, D. I., Boomer, I., Dublyansky, Y. V., Halverson,
645   G. P., Hambrey, M. J., Hendy, C., McMillan, E. A., Spötl, C., Stevenson, C. T. E., and
646   Wynn, P. M., 2016, Continental carbonate facies of a Neoproterozoic panglaciation,
647   north-east Svalbard (G. Spence, Ed.): Sedimentology, v. 63, p. 443–497.

648 Folk, R. L., 1980, Petrology of Sedimentary Rocks: Hemphill Publishing Company.

649 Frontier, S., 1976, Étude de la décroissance des valeurs propres dans une analyse en composantes
650   principales: comparison avec le modéle du bâton brisé: Journal of Experimental Marine
651   Biology, v. 25, p. 67–75.

652 Fryberger, S. G., and Schenk, C. J., 1988, Pin stripe lamination: a distinctive feature of modern
653   and ancient eolian sediments: Sedimentary Geology, v. 55, p. 1–15.

654 Goldstein, J. I., Newbury, D. E., Echlin, P., Joy, D. C., Romig Jr., A. D., Lyman, C. D., Fiori, C.,
655   and Lifshin, E., 1992, Scanning Electron Microscopy and X-Ray Microanalysis:
656   Springer.

657 Green, W. J., Stage, B. R., Bratina, B. J., Wagers, S., Preston, A., O'Bryan, K., Shacat, J., and
658   Newell, S., 2004, Nickel, Copper, Zinc and Cadmium Cycling with Manganese in Lake
659   Vanda (Wright Valley, Antarctica): Aquatic Geochemistry, v. 10, p. 303–323.

660 Gumbley, J. W., 1975, A sedimentological study of three saline lakes in the Dry Valleys of
661   Victoria Land, Antarctica [MS Thesis]: University of Waikato, 165 p.

662 Halverson, G. P., Maloof, A. C., and Hoffman, P. F., 2004, The Marinoan glaciation
663   (Neoproterozoic) in northeast Svalbard: Basin Research, v. 16, p. 297–324.

664 Halverson, G. P., 2011, Chapter 55 Glacial sediments and associated strata of the Polarisbreen
665   Group, northeastern Svalbard: Geological Society, London, Memoirs, v. 36, p. 571–579.

666 Halverson, G. P., Kunzmann, M., Strauss, J. V., and Maloof, A. C., 2018, The Tonian-
667   Cryogenian transition in Northeastern Svalbard: Precambrian Research, v. 319, p. 79–95.

668 Hoffman, P. F., and Li, Z.-X., 2009, A palaeogeographic context for Neoproterozoic glaciation:
669   Palaeogeography, Palaeoclimatology, Palaeoecology, v. 277, p. 158–172.

670 Hoffman, P. F., Halverson, G. P., Domack, E. W., Maloof, A. C., Swanson-Hysell, N. L., and
671   Cox, G. M., 2012, Cryogenian glaciations on the southern tropical paleomargin of
672   Laurentia (NE Svalbard and East Greenland), and a primary origin for the upper Russøya
673   (Islay) carbon isotope excursion: Precambrian Research, v. 206–207, p. 137–158.

674 Immonen, N., 2013, Surface microtextures of ice-rafted quartz grains revealing glacial ice in the
675   Cenozoic Arctic: Palaeogeography, Palaeoclimatology, Palaeoecology, v. 374, p. 293–
676   302.

677 Jackson, D. A., 1993, Stopping rules in principal components analysis: a comparison of
678   heuristical and statistical approaches: Ecology, v. 74, p. 2204–2214.

679 Janitsky, P., 1986, Laboratory methods: Citrate-bicarbonate-dithionite (CBD) extractable iron
680   and aluminum, *in* Field and laboratory procedures used in a soil chronosequence study:,
681   p. 38–41.

682 Jungblut, A. D., Hawes, I., Mackey, T. J., Krusor, M., Doran, P. T., Sumner, D. Y., Eisen, J. A.,
683   Hillman, C., and Goroncy, A. K., 2016, Microbial Mat Communities along an Oxygen
684   Gradient in a Perennially Ice-Covered Antarctic Lake (A. J. Stams, Ed.): Applied and
685   Environmental Microbiology, v. 82, p. 620–630.

686 Kalińska-Nartiša, E., Lamsters, K., Karušs, J., Krievāns, M., Rečs, A., and Meija, R., 2017,
687   Quartz grain features in modern glacial and proglacial environments: A microscopic
688   study from the Russell Glacier, southwest Greenland: Polish Polar Research, v. 38, p.
689   265–289.

690 Keiser, L. J., Soreghan, G. S., and Kowalewski, M., 2015, Use of Quartz Microtextural Analysis
691   To Assess Possible Proglacial Deposition For the Pennsylvanian–Permian Cutler
692   Formation (Colorado, U.S.A.): Journal of Sedimentary Research, v. 85, p. 1310–1322.

693 Kendall, B., Creaser, R. A., and Selby, D., 2006, Re-Os geochronology of postglacial black
694   shales in Australia: Constraints on the timing of "Sturtian" glaciation: Geology, v. 34, p.
695   729.

696 Kocurek, G., and Fielder, G., 1982, Adhesion structures: Journal of Sedimentary Petrology, v.
697   52, p. 1229–1241.

698 Krinsley, D., and Takahashi, T., 1962, Applications of electron microscopy to geology, *in*
699   Transactions of the New York Academy of Sciences, p. 3–22.

700 Krinsley, D. H., and Funnell, B. M., 1965, Environmental history of quartz sand grains from the
701   Lower and Middle Pleistocene of Norfolk, England: Quarterly Journal of the Geological
702   Society of London, v. 121, p. 435–456.

703 Krinsley, D., and Doornkamp, J. C., 1973, Atlas of Sand Grain Surface Textures: Cambridge
704   University Press.

705 Krinsley, D. H., and Trusty, P., 1985, Environmental interpretation of quartz grain surface
706   textures, *in* Provenance of Arenites: Springer.

707 Křížek, M., Krbcová, K., Mida, P., and Hanáček, M., 2017, Micromorphological changes as an
708   indicator of the transition from glacial to glaciofluvial quartz grains: Evidence from
709   Svalbard: Sedimentary Geology, v. 358, p. 35–43.

710 Legendre, P., and Legendre, L., 1998, Numerical ecology: Elsevier Science BV.

711 Lepper, K., and Scott, G. F., 2005, Late Holocene aeolian activity in the Cimarron River valley
712   of west–central Oklahoma: Geomorphology, v. 70, p. 42–52.

713   Lindé, K., and Mycielska-Dowgiałło, E., 1980, Some experimentally produced microtextures on
714   grain surfaces of quartz sand: Geografiska Annaleer, v. 62, p. 171–184.

715   Mackey, T. J., Sumner, D. Y., Hawes, I., Jungblut, A. D., and Andersen, D. T., 2015, Growth of
716   modern branched columnar stromatolites in Lake Joyce, Antarctica: Geobiology, v. 13, p.
717   373–390.

718   Mackey, T. J., Sumner, D. Y., Hawes, I., and Jungblut, A. D., 2017, Morphological signatures of
719   microbial activity across sediment and light microenvironments of Lake Vanda,
720   Antarctica: Sedimentary Geology, v. 361, p. 82–92.

721   Mahaney, W. C., and Kalm, V., 1995, Scanning electron microscopy of Pleistocene tills in
722   Estonia: Boreas, v. 24, p. 13–29.

723   Mahaney, W. C., Claridge, G., and Campbell, I., 1996, Microtextures on quartz grains in tills
724   from Antarctica: Palaeogeography, Palaeoclimatology, Palaeoecology, v. 121, p. 89–103.

725   Mahaney, W. C., and Kalm, V., 2000, Comparative scanning electron microscopy study of
726   oriented till blocks, glacial grains and Devonian sands in Estonia and Latvia: Boreas, v.
727   29, p. 35–51.

728   Mahaney, W. C., Stewart, A., and Volli, K., 2001, Quantification of SEM microtextures useful in
729   sedimentary environmental discrimination: Boreas, v. 30, p. 165–171.

730   Mahaney, W. C., 2002, Atlas of Sand Grain Surface Textures and Applications: Oxford
731   University Press.

732   Margolis, S. V., and Krinsley, D. H., 1971, Submicroscopic frosting on eolian and subaqueous
733   quartz sand grains: Geological Society of America Bulletin, v. 82, p. 3395–3406.

734   Margolis, S. V., and Krinsley, D. H., 1974, Processes of formation and environmental occurrence
735   of microfeatures on detrital quartz grains: American Journal of Science, v. 274, p. 449–
736   464.

737   Nartišs, M., and Kalińska-Nartiša, E., 2017, An aeolian or a glaciolacustrine record? A case
738   study from Mieļupīte, Middle Gauja Lowland, northeast Latvia: Geologos, v. 23, p. 15–
739   28.

740   Nieter, W. M., and Krinsley, D. H., 1976, The production and recognition of aeolian features on
741   sand grains by silt abrasion: Sedimentology, v. 23, p. 713–720.

742   Pedregosa, F., Varoquaux, G., Gramfort, A., Michel, V., Thirion, B., Grisel, O., Blondel, M.,
743   Prettenhofer, P., Weiss, R., Dubourg, V., Vanderplas, J., Passos, A., Cournapeau, D.,
744   Brucher, M., and others, 2011, Scikit-learn: Machine Learning in Python: Journal of
745   Machine Learning Research, v. 12, p. 2825–2830.

746   Peres-Neto, P. R., Jackson, D. A., and Somers, K. M., 2003, Giving meaningful interpretation to
747   ordination axes: assessing loading significance in principal component analysis: Ecology,
748   v. 84, p. 2347–2363.

749   Pettijohn, F. J., 1957, Paleocurrents of Lake Superior Precambrian quartzites: Bulletin of the
750   Geological Society of America, v. 68, p. 469–480.

751   Pippin, M., 2016, Progressive downstream overprinting of glacially induced quartz microtextures
752   during fluvial saltation, Salmon River, British Columbia and Alaska [MS Thesis]: Texas
753   Tech University, 85 p.

754   Porter, J. J., 1962, Electron microscopy of sand surface texture: Journal of Sedimentary
755   Petrology, v. 32, p. 124–135.

756   Prave, A. R., Condon, D. J., Hoffmann, K. H., Tapster, S., and Fallick, A. E., 2016, Duration and
757   nature of the end-Cryogenian (Marinoan) glaciation: Geology, v. 44, p. 631–634.

758   Pye, K., 1983, Coastal Dunes: Progress in Physical Geography, v. 7, p. 531–557.

759   Pye, K., and Tsoar, H., 2009, Aeolian sand and sand dunes: Springer, 458 p.

760   Říha, K., Křupka, A., and Costa, P. J. M., 2019, Image analysis applied to quartz grain
761   microtextural provenance studies: Computers & Geosciences, v. 125, p. 98–108.

762   Rose, C. V., Maloof, A. C., Schoene, B., Ewing, R. C., Linnemann, U., Hofmann, M., and
763   Cottle, J. M., 2013, The End-Cryogenian Glaciation of South Australia: Geoscience
764   Canada, v. 40, p. 256.

765   Runkel, A. C., Mackey, T. J., Cowan, C. A., and Fox, D. L., 2010, Tropical shoreline ice in the
766   late Cambrian: Implications for Earth's climate between the Cambrian Explosion and the
767   Great Ordovician Biodiversification Event: GSA Today, p. 4–10.

768   Schelp, C., 2019, An Alternative Way to Plot the Covariance Ellipse, at CarstenSchelp.github.io
769   at https://carstenschelp.github.io/2018/09/14/Plot_Confidence_Ellipse_001.html.

770   Setlow, L. W., 1978, Age determination of reddened coastal dunes in northwest Florida, U.S.A.,
771   by use of scanning electron microscopy, *in* Scanning electron microscopy in the study of
772   sediments: Geo Abstracts, p. 283–305.

773   Shacat, J. A., Green, W. J., DeCarlo, E. H., and Newell, S., 2004, The Geochemistry of Lake
774   Joyce, McMurdo Dry Valleys, Antarctica: Aquatic Geochemistry, v. 10, p. 325–352.

775   Smith, C., Soreghan, G. S., and Ohta, T., 2018, Scanning electron microscope (SEM)
776   microtextural analysis as a paleoclimate tool for fluvial deposits: A modern test: GSA
777   Bulletin, v. 130, p. 1256–1272.

778   Spigel, R. H., and Priscu, J. C., 1998, Physical limnology of the McMurdo Dry Valleys Lakes, *in*
779   Ecosystem Dynamics in a Polar Desert: the McMurdo Dry Valleys, Antarctica: American
780   Geophysical Union, p. 153–187.

781   Stevic, M., 2015, Identification and environmental interpretation of microtextures on quartz
782   grains from aeolian sediments - Brattforsheden and Vittskövle, Sweden [BS Thesis]:
783   Lund University, 35 p.

784   Stokes, S., Kocurek, G., Pye, K., and Winspear, N. R., 1997, New evidence for the timing of
785   aeolian sand supply to the Algodones dunefield and East Mesa area, southeastern
786   California, USA: Palaeogeography, Palaeoclimatology, Palaeoecology, v. 128, p. 63–75.

787   Sweet, D. E., and Soreghan, G. S., 2010, Application of quartz sand microtextural analysis to
788   infer cold-climate weathering for the equatorial Fountain Formation (Pennsylvanian-
789   Permian, Colorado, U.S.A.): Journal of Sedimentary Research, v. 80, p. 666–677.

790   Sweet, D. E., and Brannan, D. K., 2016, Proportion of Glacially To Fluvially Induced Quartz
791   Grain Microtextures Along the Chitina River, SE Alaska, U.S.A.: Journal of Sedimentary
792   Research, v. 86, p. 749–761.

793   Vincent, P. J., 1976, Some periglacial deposits near Aberystwyth, Wales, as seen with a scanning
794   electron microscope: Biuletyn Periglacialny, v. 25, p. 59–64.

795   Vos, K., Vandenberghe, N., and Elsen, J., 2014, Surface textural analysis of quartz grains by
796   scanning electron microscopy (SEM): From sample preparation to environmental
797   interpretation: Earth-Science Reviews, v. 128, p. 93–104.

798   Williams, G. E., 1998, Late Neoproterozoic periglacial aeolian sand sheet, Stuart Shelf, South
799   Australia*: Australian Journal of Earth Sciences, v. 45, p. 733–741.

800   Wilson, I. G., 1972, Aeolian bedforms—their development and origins: Sedimentology, v. 19, p.
801   173–210.

802   Winspear, N. R., and Pye, K., 1995, Sand supply to the Algodones dunefield, south-eastern
803   California, USA: Sedimentology, v. 42, p. 875–891.

804   Woronko, B., 2016, Frost weathering versus glacial grinding in the micromorphology of quartz
805   sand grains: Processes and geological implications: Sedimentary Geology, v. 335, p.
806   103–119.

807   Yu, W., Algeo, T. J., Du, Y., Zhou, Q., Wang, P., Xu, Y., Yuan, L., and Pan, W., 2017, Newly
808   discovered Sturtian cap carbonate in the Nanhua Basin, South China: Precambrian
809   Research, v. 293, p. 112–130.

810   Zhang, S., Jiang, G., and Han, Y., 2008, The age of the Nantuo Formation and Nantuo glaciation
811   in South China: Terra Nova, v. 20, p. 289–294.